Science

RESEARCH ARTICLES

Cite as: Y. Guo *et al.*, *Science*
10.1126/science.ady9404 (2026).

Deeper detection limits in astronomical imaging using self-supervised spatiotemporal denoising

Yuduo Guo[1,2,3]†, Hao Zhang[1,2,3]†, Mingyu Li[4]†, Fujiang Yu[4], Yunjing Wu[4,5], Yuhan Hao[1,2,3], Song Huang[4], Yongming Liang[6,7], Xiaojing Lin[4], Xinyang Li[8], Jiamin Wu[1,2,3]*, Zheng Cai[4,9,10]*, Qionghai Dai[1,2,3]*

[1]Department of Automation, Tsinghua University, Beijing, China. [2]Beijing National Research Center for Information Science and Technology, Tsinghua University, Beijing, China. [3]Institute for Brain and Cognitive Sciences, Tsinghua University, Beijing, China. [4]Department of Astronomy, Tsinghua University, Beijing, China. [5]Kavli Institute for the Physics and Mathematics of the Universe, The University of Tokyo, Kashiwa, Japan. [6]National Astronomical Observatory of Japan, Tokyo, Japan. [7]Institute for Cosmic Ray Research, The University of Tokyo, Kashiwa, Japan. [8]College of Artificial Intelligence, Tsinghua University, Beijing, China. [9]School of Mathematics and Physics, Qinghai University, Xining, China. [10]Tsinghua Wuxi Institute of Applied Technology, Wuxi, China.

†These authors contributed equally to this work

***Corresponding author. Email: qhdai@tsinghua.edu.cn (Q. D.); zcai@tsinghua.edu.cn (Z. C.); wujiamin@tsinghua.edu.cn (J.W.)**

The detection limit of astronomical imaging observations is limited by several noise sources. Some of that noise is correlated between neighboring pixels and exposures, so in principle could be learned and corrected. We present the Astronomical Self-supervised Transformer-based Denoising (ASTERIS) algorithm, which integrates spatiotemporal information across multiple exposures. Benchmarking on mock data indicates that ASTERIS improves detection limits by 1.0 magnitude at 90% completeness and purity, while preserving the point spread function and photometric accuracy. Observational validation using data from the James Webb Space Telescope (JWST) and Subaru telescope identifies previously undetectable features, including low-surface-brightness galaxy structures and gravitationally-lensed arcs. Applied to deep JWST images, ASTERIS identifies three times more redshift $\gtrsim 9$ galaxy candidates than previous methods, with rest-frame ultraviolet luminosity 1.0 magnitude fainter.

The imaging detection limit in observational astronomy determines how faint an object can be observed with a given instrument and exposure time (*1*–*3*). It is limited by noise from the instrument (*4*–*7*), sky background (*8*), and photon statistics (*9*). Larger-aperture telescopes and advanced instrumentation can collect more photons, reduce instrumental readout noise, and thus improve the signal-to-noise ratio (S/N) of the resulting image (*10*–*12*). However, other sources of background noise—such as those from zodiacal emission, Galactic foregrounds (*13*), and atmospheric scattering (*8*)—cannot be corrected by those advances in hardware.

Software signal processing algorithms have been used to improve the S/N in astronomical imaging. A widely adopted method involves aligning and co-adding multiple exposures. If there are M exposures, each in the background-dominated regime, this theoretically improves the S/N by a factor of $\sqrt{M}$ (Fig. 1A), assuming the pixel-level noise is independent and identically distributed (i.i.d.) (*14*–*16*). However, this approach provides diminishing returns for deep surveys, because the required exposure time scales prohibitively with increasing depth. Taking the James Webb Space Telescope (JWST) as an example, increasing its 5σ detection limit (where σ is the standard deviation of the noise) from 31 to 32 magnitudes (mag, on the AB system unless otherwise stated; higher numbers are fainter) in the F115W band (this notation indicates a wideband filter centered at 1.15 μm) would require increasing the total exposure time from 4 days to approximately one month (*17*). Convolution with a smoothing kernel can also improve the detection limit (*18*, *19*), by reinforcing local pixel correlations and suppressing high-frequency noise. However, smoothing methods inevitably degrade the spatial resolution.

Deep learning algorithms have been employed in denoising techniques for astronomy (*20*–*23*). Supervised deep denoising methods utilize machine learning trained on pairs of noisy and clean images, from single (*24*) or multiple exposures (*25*, *26*). In astronomy, such image pairs are typically generated synthetically (*21*) or through paired long and short exposures (*22*, *23*). The effectiveness of these methods is limited by substantial differences between synthetic and real data, coupled with the complexity and variability of noise in astronomical imaging. Collection of long and short exposure pairs is constrained by the limited observing time available, restricting the availability of reliable training data.

Alternative self-supervised methods require only a single image (*20*, *27*–*29*) or pairs of noisy images (*21*) for training; several of these methods are based on the Noise2Noise (N2N) algorithmic framework (*30*). These methods typically rely on the overall image S/N as the primary performance metric, which does not necessarily describe the practical improvement for astronomical applications. These methods can introduce artefacts and miss real sources after processing, even in images that appear to be visually clean (*31*).

To mitigate cosmic ray hits, pixel saturation, and spatially varying background emission, astronomical imaging observations typically adopt multiple dithered exposures (*32*). Co-addition (also known as stacking) methods average pixel values across the multiple exposures, while rejecting outlier pixel values (Fig. 1A). However, the assumption that noise is pixel-level i.i.d. is generally violated in real data, due to spatial correlations introduced by the telescope's point spread function (PSF), structured background emission, and instrumental effects. Therefore, in practice co-addition methods do improve the S/N, but a deeper detection limit might theoretically be achievable. Algorithms that capture spatial correlations could further improve the performance after co-addition. For example, N2N-based methods (*30*) employ convolutional neural networks (CNNs) to capture local spatial correlations in a single co-added image, providing improved noise suppression (Fig. 1A).

Concept, design and implementation

We extended the N2N concept of single-image denoising, to multiple exposures of the same target field. We designed a machine learning algorithm, which we name Astronomical Self-supervised Transformer-based Denoising (ASTERIS), to exploit the spatiotemporal correlations between multiple exposures, with the goal of producing a higher-S/N image during the co-addition process of a stack of exposures. The algorithm is applied after conventional imaging data reduction but before the identification of sources in the image (Fig. 1A).

ASTERIS employs a tailored spatiotemporal learning strategy, using a dedicated attention mechanism to fuse structured voxel (two-dimensional image pixels with a third dimension representing the multiple exposures) information in exposures that are astrometrically aligned to the same world coordinate system (WCS). Figure S1A shows the detailed neural network architectures we adopted.

For self-supervised training, ASTERIS requires a total of 16 astrometrically aligned exposures of the same field. These are divided into two independent sets: an input set and a target set, each containing eight exposures. Both sets share the same underlying signal expectation but have independent noise realizations (*33*). By minimizing the loss function between the two sets, the neural network learns to estimate the signal expectation of the input set exposures using the target set exposures as a proxy for a clean reference image. For the loss function, we adopt a composite of two components: (a) the mean squared error (MSE) between the co-addition of the input set and the target set (the average loss), and (b) the mean absolute error (MAE) calculated between individual corresponding exposures from each set (the frame loss). We investigated different loss functions and found that this approach reduces complex background noise, preserves faint astronomical signals that would otherwise be buried beneath local noise fluctuations, and reduces false positive detections (*33*). Once the neural network has been trained using these 16 exposures, the algorithm can perform denoising on any eight input exposures from the same instrument [chosen based on the number of exposures typically used in JWST deep imaging surveys (*32*)], without requiring additional reference data. This algorithmic framework can also accommodate different numbers of input exposures, as discussed below.

Given the wide dynamic range of most astronomical imaging observations, and because noise primarily affects faint sources, ASTERIS selectively operates on the fainter parts of each image. Specifically, we impose an input flux threshold of 3σ significance above the background noise, chosen for practical reasons (*33*). Pixels below this threshold are retained for denoising by the neural network, while pixels above 3σ are temporarily clipped, median combined and later directly re-integrated into the final image. This approach preserves the original dynamic range without introducing a discontinuity in flux values (Fig. 1, B to D, and figs. S2 and S3). Imposing this threshold concentrates the neural network's learning capacity on low-S/N parts of the image, thereby optimizing for faint-source detection and characterization.

Algorithmic performance

To quantitatively evaluate the performance of ASTERIS, we developed an evaluation pipeline using mock data, an established method in observational astronomy. To generate the mock data, we utilize real images in the F115W filter taken from the JWST GLIMPSE (Gravitational Lensing & NIRCam Imaging to Probe Early Galaxy Formation and Sources of Reionization) program (*34*), which obtained 168 dithered exposures at a single pointing. We injected mock sources into the real data (table S2), then tested their recovery using ASTERIS. This approach ensures the independence and variability of background realizations.

The images were resampled to a pixel scale of 0.04 arcseconds (″), then a source-free 128 × 128-pixel region was selected as the background. We generated 2000 independent background realizations by randomly selecting sets of eight exposures from the 168 available images ($\approx 6 \times 10^{15}$ possible combinations; fig. S4A). This ensures that the set of realizations are statistically independent and avoids sampling bias. Astronomical observations typically assess their completeness for point sources, so we inject 25 isolated mock point sources in each background realization, for a total of 50,000 mock sources. The assumed distribution of mock source properties followed a cubic power-law from 27.5 to 31.5 mag (fig. S4B). For the mock testing, we used an ASTERIS model that was trained on real JWST data from four other observing programs (*33*), which converged in approximately 10 epochs

(~ 26 hours). Inference on each 8-exposure 1650 × 1650-pixel image stack required ~ 18.1 s to generate a denoised 1650 × 1650-pixel output image, using 4 graphics processing units (GPUs, each with 40 GB of GPU memory). Detailed computational costs are discussed in the supplement (*33*).

To assess the performance of ASTERIS (trained on JWST data; table S1), we compared the results to existing methods, including: co-addition (outlier-rejected averaging); Gaussian smoothing (*18*); Block-Matching and 3D Filtering (BM3D) (*35*); Block-Matching and 4D Filtering (BM4D) (*36*); Neighbor2Neighbor (*27*); and N2N (*30*) (fig. S5). We used the version of N2N implemented using the Restormer architecture (*37*), similar to that used in ASTERIS. Sources were identified in the output image produced by each method using the Source Extractor software (*38*), in an identical configuration (*33*). We find that ASTERIS consistently yields narrower image histograms, indicating lower noise standard deviation, and more true positive sources (see Fig. 2, B to D, which compare ASTERIS to co-addition and N2N). We calculate the source-dependent photometric S/N using circular apertures of 0.14″ radius, which enclose approximately 80% of the PSF flux in these JWST data (fig. S4C). Using this metric, the resulting 5σ sensitivity provided by N2N is an improvement over co-addition, and ASTERIS is an improvement over N2N (Fig. 2E).

The photometric S/N, which quantifies visual performance, does not fully capture the practical improvements in astronomical applications. We performed an analysis of source completeness (the fraction of true sources that are correctly detected) and purity (the fraction of detections that are true positive sources) (*33*), which are commonly employed to quantify detection performance in astronomical imaging. At the 90% completeness level, N2N improves the detection limit by 0.1 mag compared to co-addition, while ASTERIS improves it by about 1.0 mag (Fig. 2F). At 90% purity, ASTERIS improves by more than 1.5 mag compared to co-addition, and 1.0 mag compared to N2N, indicating a concurrent reduction in false positives (Fig. 2G). When evaluated using the F-score metric (equation S7), which combines completeness and purity (*33*), ASTERIS improves the limiting depth at F-score = 0.9 by about 1.7 mag compared to co-addition (Fig. 2H) and 1.4 mag compared to N2N (fig. S5K). We find similar improvements under less controlled conditions, with a larger field and bright sources masked out (fig. S6), which more closely resemble real observations. We also performed quantitative analyses of the performance variations resulting from different combinations of loss functions during training (fig. S7) and different flux thresholds for the sigma-clipping method used in ASTERIS (fig. S8).

To investigate the effect of ASTERIS on spatial resolution and photometric measurements, we evaluated the PSF fidelity and photometric accuracy (*33*). We derived the PSF profiles output by each method using the radially averaged flux around the extracted PSF centers (Fig. 2I). A two-sample Kolmogorov–Smirnov test (*39*) comparing the PSF profiles from ASTERIS and co-addition yielded a p-value of 0.9, indicating no statistically significant difference between them. In contrast, the same test for N2N yielded a statistically significant $p < 0.05$, which we interpret as indicating degraded resolution in the N2N output. We performed additional tests of photometric accuracy (*33*), finding no evidence of systematic biases introduced by ASTERIS, and slightly improved photometric precision for faint sources, compared to co-addition (Fig. 2J). We also verified that the ASTERIS output is robust to the permutation order of the input exposures (figs. S9 and S10).

Observational validation and generalization

Detecting faint sources or low-surface-brightness features (*40*) is challenging in astronomical imaging. We evaluate the performance of ASTERIS for this task (*33*), using the same trained model as in Fig. 2. We use space-based JWST data, and ground-based data from the Subaru telescope, to assess the generalization capability of the algorithm. All the data used for testing was excluded from the training dataset (table S1).

We again utilize NIRCam data from the JWST GLIMPSE program (*34*): eight exposures (independent from the training data) for co-addition benchmarking and ASTERIS denoising, and a deep co-addition of 168 exposures serving as ground truth. For this test, ASTERIS utilized not only information derived from the eight exposures, but also the statistical priors previously learned from the training datasets (table S1), which used the same instrument. This test was applied to observations taken in three filters: F115W (Fig. 3, A to F, and J to L), F090W (Fig. 3, G to I), and F444W (Fig. 3, M to O).

For faint sources, especially those in a crowded field near bright sources (*41*), the presence of spatially complex background noise compromises both source detection and accurate flux estimation (Fig. 3A and fig. S11A). We analyzed a representative crowded field, which contains numerous faint sources that were undetected in a standard co-addition of the 8-exposure NIRCam stack, but were detected in the 168-exposure co-addition of the same field. Using Source Extractor, we identify 169 sources in the 168-exposure image (Fig. 3C and fig. S11C), of which 97 are recovered by ASTERIS from the 8-exposure input (fig. S11B). We verified that the cross-matched sources are true positives and preserve photometric accuracy (Fig. 3, B to F). In contrast, the conventional 8-exposure co-addition recovers only 50 of these sources (fig. S11A) under identical Source Extractor settings. When ASTERIS is applied directly to the full 168 exposures, 229 sources are detected (Fig. 3D and fig. S11D), 35% more than were identified using standard methods. This demonstrates that ASTERIS can identify additional sources in an existing dataset, without the need for additional exposure time or hardware upgrades. We verified this conclusion (fig. S12) using imaging data from another JWST program (*42*).

To investigate low-surface-brightness features, we consider the extended stellar disks and diffuse outer arms of spiral galaxies (*43*, *44*), which are often undetectable in observations (Fig. 3, G to I, and fig. S13B). We apply ASTERIS to F090W data from the JWST GLIMPSE program and calculate the structural similarity (SSIM) metric (*45*), which quantifies the suitability of an image for morphological characterization of galaxies. For an 8-exposure co-addition, we find that ASTERIS improves the SSIM value from 0.37 (Fig. 3G) to 0.67 (Fig. 3H), compared to standard methods. In the same image, we find that ASTERIS also improved the reconstruction of a low-surface-brightness gravitationally lensed arc (Fig. 3, J to L, and fig. S13D), the distorted image of a distant galaxy (*46*). For this lensed arc, the SSIM increases from 0.59 using standard co-addition (Fig. 3J) to 0.81 using ASTERIS (Fig. 3K). We find similar improvements in the identification of groups of faint and diffuse galaxies (Fig. 3, M to O, and fig. S13F).

To investigate whether ASTERIS generalizes to data from different instruments, we utilize observations from the ground-based Subaru telescope using the Multi-Object Infrared Camera and Spectrograph (MOIRCS) (*47*, *48*). Compared to the space-based JWST data, these observations have lower spatial resolution due to atmospheric turbulence (seeing), and higher sky background noise (Fig. 3P). Directly applying the JWST-trained model leads to some false positive sources (fig. S14B). We therefore trained a dedicated ASTERIS model using Subaru datasets from three observing programs (*33*, *49*). This was used for a similar test to the JWST data, applying ASTERIS to a stack of eight 3-s Subaru exposures, and comparing the results to a deeper (2088 s) co-added exposure of the same field (Fig. 3R) using the same instrument in the same *Ks* band (short *K*, a near-infrared filter centered at 2.15 μm). We find that ASTERIS recovers the faint sources in this ground-based data (Fig. 3Q and fig. S13H).

Application to faint high-redshift galaxies

As an example application of ASTERIS, we search for high-redshift galaxies, the most distant and earliest known galaxies with extremely faint apparent magnitudes. We employ ASTERIS to process images from the JWST Advanced Deep Survey (JADES), in the JADES Origins Field (JOF) (*50*, *51*). This dataset uses 14 filters from F090W to F444W (table S1). Previous studies have identified a population of high-redshift galaxy candidates in the JOF, with redshifts $z \sim 9$ to 15 (some with only a photometric redshift z_{phot}, others with a spectroscopically confirmed redshift), with the faintest having rest-frame ultraviolet (UV) absolute magnitudes $M_{\mathrm{UV}} = -17$ (*52*, *53*). We run ASTERIS on the JOF data, identify sources using Source Extractor, and select high-redshift galaxy candidates (*33*) using criteria that are consistent with previous work (*53*).

The 5σ depth of the JOF in previous work was 30.3 to 30.8 mag, varying between the 14 bands (*53*). We find this improves to 30.9 to 31.6 mag using ASTERIS (fig. S15). We identify 162 high-redshift galaxy candidates at $z_{\mathrm{phot}} \gtrsim 9$, which is approximately three times the number previously identified (table S3, Fig. 4, and fig. S16). The faintest candidates we identify have $M_{\mathrm{UV}} \approx -16$ mag, one magnitude fainter than in previous studies. ASTERIS recovers all the high-redshift galaxies in JOF that have been spectroscopically confirmed by previous work (*1*), or were identified as candidates by multiple previous works (*52*, *53*). 75% of the high-redshift galaxy candidates identified using ASTERIS were not previously reported (*52*, *53*). Table S3 and data S1 list the measured M_{UV} and photometric redshifts for all the candidate sources. We assessed the detection and selection completeness using source-injection simulations (fig. S17) (*33*).

We ascribe this threefold expansion in the number of identified candidates to two primary effects of ASTERIS. First, ASTERIS enables the detection of fainter sources, with apparent magnitude of 31 to 32 (Fig. 5, A and B). By suppressing the noise, ASTERIS improves the detection limit, allowing previously marginal signals to become detections. Secondly, the improved S/N for faint sources helps to resolve ambiguities in the photometric redshift of each source (Fig. 5, C and D). High-redshift galaxy candidates are selected using the Lyman-break technique (*54*), in which intervening neutral hydrogen in the intergalactic medium absorbs UV light blueward of the Lyman-α line (1215.6 Å). The wavelength of this break is redshifted into the near-infrared for $z \gtrsim 9$ objects, causing them to appear bright in longer-wavelength filters but remain invisible in shorter-wavelength filters (referred to as a dropout). Therefore, a strong break or non-detection ($S/N < 2$) of galaxies at wavelengths shorter than rest-frame 1215.6 Å serves as the primary indicator of a high-redshift source. However, some low-redshift galaxies have a similar break at the shorter rest-frame wavelength 0.4 μm due to the Balmer break (*55*, *56*). If the brightness of those sources is similar to the noise level, a low-redshift Balmer break can be misidentified as a high-redshift Lyman break, or the data are unable to distinguish between these two possibilities. ASTERIS reduces this effect by providing deeper detection limits in the dropout bands, thereby better constraining the source photometric redshift, particularly for sources that were marginally significant ($S/N \sim 2$) using standard co-addition methods (Fig. 5D).

The JOF field contains some even higher redshift galaxy candidates ($z > 16$) which were not identified by previous works (*52*, *53*). Our analysis using ASTERIS identifies four candidates with $z \sim 16$ to 22.5 (table S3). Figure 5E shows an example dropout in the F200W band. The redshift probability distribution for this source derived using ASTERIS (fig. S18A) shows the high-redshift solution ($z_{\mathrm{phot}} = 17.08$; Fig. 5E) is far more probable than the alternative low-redshift solution (fig. S18B).

We use the identified galaxy candidates to quantify the rest-frame UV luminosity functions, which describe the number density of galaxies with different luminosities in selected redshift bins. The ASTERIS analysis identified 125 galaxy candidates at $z \sim 9$ to 12, and 33 galaxy candidates at $z \sim 12$ to 16, within an observed volume that is substantially smaller than previous studies (*52*, *53*). Figure 6 shows the resulting UV luminosity functions, which we fitted with models (*33*) that have steep faint-end slopes of -2.45 ± 0.03 for $z \sim 9$ to 12 and -2.28 ± 0.02 for $z \sim 12$ to 16. These values indicate higher number densities of faint galaxies ($M_{\mathrm{UV}} \gtrsim -16$) than were predicted by theoretical models (*57*, *58*).

Extension to different numbers of exposures

Due to the neural network architecture (fig. S1), ASTERIS requires an even number of input exposures. Our choice of an 8-exposure input in ASTERIS was made based on the recommended observing strategy for deep JWST surveys (typically 9-point dithers) (*32*) while balancing the neural network's memory requirements and computational efficiency. To test its applicability to other survey strategies, we also developed a 4-exposure variant of ASTERIS (*33*). Compared to the 8-exposure version, the 4-exposure neural network provides a smaller improvement in detection limit—from 1.0 mag to 0.7 mag at 90% completeness—with a corresponding decrease in the identification of faint sources (fig. S19). We attribute this degradation to the reduced availability of spatiotemporal information in the smaller number of exposures.

We strongly discourage artificially duplicating exposures to increase the number of input exposures, because this would violate the assumptions required for the spatiotemporal learning strategy. Our tests of this approach (*33*) show it increases the false positive rate (fig. S20). In the opposite situation, where more exposures are available than accepted by ASTERIS, they can be grouped into subsets and each subset combined (via co-addition) to produce the required number of exposures. For example, a set of 24 exposures can be co-added in eight subsets of three exposures each, then the eight combined exposures used as input for ASTERIS (fig. S21A). We also tested situations where the number of available exposures is not a simple multiple of those used by ASTERIS, such as 21 exposures used by the 8-exposure version of ASTERIS (fig. S21B), or seven exposures used by the 4-exposure version of ASTERIS (fig. S21C).

Methods summary

For training and testing ASTERIS, we used JWST NIRCam imaging data from programs 3293 (*34*), 1210, 3215 (*50*, *51*), 1963 (*59*), and 4111 (*42*), spanning filters from F070W to F480M (the latter is a medium band filter centered at 4.80 μm). We reduced these data using the JWST Science Calibration Pipeline v1.15.1 (*60*), with additional procedures as previously recommended to mitigate instrumental artifacts (*61*, *62*). Astrometric calibration of the exposures was performed using published catalogs (*50*, *63*). We combined astrometrically aligned individual exposures along the temporal domain to form a 3D data cube, then applied a 3σ clipping to separate the cube into a faint part and a bright part. Only the faint part was used for ASTERIS training and was Z-score normalized (equation. S4) prior to being input into the neural network.

The neural network architecture of ASTERIS utilizes a spatiotemporal 3D U-Net framework, enhanced with multi-deconvolved head-transposed attention, to overcome the receptive field limitations of traditional CNNs. We trained ASTERIS separately for the long-wavelength (filter central wavelength ≥ 2.5 μm) and short-wavelength (< 2.5 μm) NIRCam imaging data. The loss function comprised a weighted combination of MSE and MAE losses (equations S1-S3). The training dataset was segmented into 120,000 patches (60,000 pairs) with each patch formatted as an $8 \times 128 \times 128$ pixel data cube. The training reached convergence in approximately 10 iterations (~26 hours).

For denoising, ASTERIS partitions input exposures into patches according to the specified patch size and the number of available GPUs. We benchmarked ASTERIS against previous denoising methods using the injection of mock sources into the JWST NIRCam F115W data, using a model PSF generated with the STPSF software (*64*). These mock sources, ranging from 27.5 to 31.5 mag, followed a third-order power-law distribution, to match the source counts in the real observations. We quantified the performance using metrics including completeness, purity, and the F-score (equation S7) (*65*, *66*). The output PSF from the different methods was extracted using the PSFEx software (*67*) and its profile analyzed using radial averaging. Photometric accuracy was investigated through forced-aperture photometry at known mock-source locations.

The trained ASTERIS was then applied to identify faint high-redshift galaxy candidates within the JOF (*50*, *51*). Source detection was performed using Source Extractor (*38*) on a composite detection image generated by co-adding the ASTERIS-denoised images in F277W, F356W and F444W. We conducted forced-aperture photometry with a 0.1″ radius circular aperture across all filters, applying aperture corrections based on PSF profiles and the flux ratio between circular and Kron photometry (*68*). The photometric uncertainties were estimated using random aperture sampling (same radius as used in photometry) on source-free regions. We adapted the criteria from previous work (*53*) for high-redshift galaxy candidate selection, followed by a preliminary spectral energy distribution (SED) fitting using the EAZY software (*69*) and a suite of template spectra (*70*). The physical properties of the candidates were inferred with the Bayesian Analysis of Galaxy SEDs (BEAGLE) software (*71*) using pre-existing models (*53*). Binned luminosity functions were calculated using the effective volume method (*72*) (equations S8-S9) and characterized by fitting a Schechter function (*73*). Their completeness was evaluated using mock source injection and recovery tests.

REFERENCES AND NOTES

1. S. Carniani, K. Hainline, F. D'Eugenio, D. J. Eisenstein, P. Jakobsen, J. Witstok, B. D. Johnson, J. Chevallard, R. Maiolino, J. M. Helton, C. Willott, B. Robertson, S. Alberts, S. Arribas, W. M. Baker, R. Bhatawdekar, K. Boyett, A. J. Bunker, A. J. Cameron, P. A. Cargile, S. Charlot, M. Curti, E. Curtis-Lake, E. Egami, G. Giardino, K. Isaak, Z. Ji, G. C. Jones, N. Kumari, M. V. Maseda, E. Parlanti, P. G. Pérez-González, T. Rawle, G. Rieke, M. Rieke, B. R. Del Pino, A. Saxena, J. Scholtz, R. Smit, F. Sun, S. Tacchella, H. Übler, G. Venturi, C. C. Williams, C. N. A. Willmer, Spectroscopic confirmation of two luminous galaxies at a redshift of 14. *Nature* **633**, 318–322 (2024). doi:10.1038/s41586-024-07860-9 Medline
2. E. Zackrisson, C. E. Rydberg, D. Schaerer, G. Östlin, M. Tuli, The spectral evolution of the first galaxies. I. James Webb space telescope detection limits and color criteria for population III galaxies. *Astrophys. J.* **740**, 13 (2011). doi:10.1088/0004-637X/740/1/13
3. J. M. Helton, G. H. Rieke, S. Alberts, Z. Wu, D. J. Eisenstein, K. N. Hainline, S. Carniani, Z. Ji, W. M. Baker, R. Bhatawdekar, A. J. Bunker, P. A. Cargile, S. Charlot, J. Chevallard, F. D'Eugenio, E. Egami, B. D. Johnson, G. C. Jones, J. Lyu, R. Maiolino, P. G. Pérez-González, M. J. Rieke, B. Robertson, A. Saxena, J. Scholtz, I. Shivaei, F. Sun, S. Tacchella, L. Whitler, C. C. Williams, C. N. A. Willmer, C. Willott, J. Witstok, Y. Zhu, Photometric detection at 7.7 μm of a galaxy beyond redshift 14 with JWST/MIRI. *Nat. Astron.* **9**, 729–740 (2025). doi:10.1038/s41550-025-02503-z Medline
4. J. W. MacKenty, S. M. Baggett, G. Brammer, B. Hilbert, K. S. Long, P. McCullough, A. G. Riess, "HST/WFC3: New capabilities, improved IR detector calibrations, and long-term performance stability" in *Space Telescopes and Instrumentation 2014: Optical, Infrared, and Millimeter Wave*, J. M. Oschmann Jr., M. Clampin, G. G. Fazio, H. A. MacEwen, Eds. (SPIE, 2014), vol. 9143, pp. 655–667; https://doi.org/10.1117/12.2056853.
5. J. E. Gunn, M. Carr, C. Rockosi, M. Sekiguchi, K. Berry, B. Elms, E. de Haas, Ž. Ivezić, G. Knapp, R. Lupton, G. Pauls, R. Simcoe, R. Hirsch, D. Sanford, S. Wang, D. York, F. Harris, J. Annis, L. Bartozek, W. Boroski, J. Bakken, M. Haldeman, S. Kent, S. Holm, D. Holmgren, D. Petravick, A. Prosapio, R. Rechenmacher, M. Doi, M. Fukugita, K. Shimasaku, N. Okada, C. Hull, W. Siegmund, E. Mannery, M. Blouke, D. Heidtman, D. Schneider, R. Lucinio, J. Brinkman, The Sloan Digital Sky Survey Photometric Camera. *Astron. J.* **116**, 3040–3081 (1998). doi:10.1086/300645
6. T. Ichikawa, R. Suzuki, C. Tokoku, Y. Katsuno Uchimoto, M. Konishi, T. Yoshikawa, T. Yamada, I. Tanaka, K. Omata, T. Nishimura, "MOIRCS: multi-object infrared camera and spectrograph for SUBARU" in *Ground-Based and Airborne Instrumentation for Astronomy*, I. S. McLean, M. Iye, Eds. (SPIE, 2006), vol. 6269, pp. 397–408; https://doi.org/10.1117/12.670078.
7. S. D. Horner, M. J. Rieke, "The near-infrared camera (NIRCam) for the James Webb Space Telescope (JWST)" in *Optical, Infrared, and Millimeter Space Telescopes*, J. C. Mather, Ed. (SPIE, 2004), vol. 5487, pp. 628–634; https://doi.org/10.1117/12.552281.
8. R. H. Garstang, Night-sky brightness at observatories and sites. *Publ. Astron. Soc. Pac.* **101**, 306 (1989). doi:10.1086/132436
9. Ya. M. Blanter, M. Büttiker, Shot noise in mesoscopic conductors. *Phys. Rep.* **336**, 1–166 (2000). doi:10.1016/S0370-1573(99)00123-4
10. I. S. McLean, *Electronic Imaging in Astronomy: Detectors and Instrumentation* (Springer, ed. 2, 2008).
11. M. V. Zombeck, *Handbook of Space Astronomy and Astrophysics* (Cambridge Univ. Press, ed. 3, 2006).
12. F. R. Chromey, *To Measure the Sky: An Introduction to Observational Astronomy* (Cambridge Univ. Press, ed. 2, 2016).
13. J. R. Rigby, P. A. Lightsey, M. García Marín, C. W. Bowers, E. C. Smith, A. Glasse, M. W. McElwain, G. H. Rieke, R.-R. Chary, X. C. Liu, M. Clampin, R. A. Kimble, W. Kinzel, V. Laidler, K. I. Mehalick, A. Noriega-Crespo, I. Shivaei, D. Skelton, C. Stark, T. Temim, Z. Wei, C. J. Willott, How dark the sky: The JWST backgrounds. *Publ. Astron. Soc. Pac.* **135**, 048002 (2023). doi:10.1088/1538-3873/acbcf4
14. J. Annis, M. Soares-Santos, M. A. Strauss, A. C. Becker, S. Dodelson, X. Fan, J. E. Gunn, J. Hao, Ž. Ivezić, S. Jester, L. Jiang, D. E. Johnston, J. M. Kubo, H. Lampeitl, H. Lin, R. H. Lupton, G. Miknaitis, H.-J. Seo, M. Simet, B. Yanny, The Sloan Digital Sky Survey Coadd: 275 deg^2 of deep Sloan Digital Sky Survey Imaging on stripe 82. *Astrophys. J.* **794**, 120 (2014). doi:10.1088/0004-637X/794/2/120
15. R. R. R. Reis, M. Soares-Santos, J. Annis, S. Dodelson, J. Hao, D. Johnston, J. Kubo, H. Lin, H.-J. Seo, M. Simet, The Sloan Digital Sky Survey Co-add: A galaxy photometric redshift catalog. *Astrophys. J.* **747**, 59 (2012). doi:10.1088/0004-637X/747/1/59
16. J. Bosch, Y. AlSayyad, R. Armstrong, E. Bellm, H.-F. Chiang, S. Eggl, K. Findeisen, M. Fisher-Levine, L. P. Guy, A. Guyonnet, Ž. Ivezic, T. Jenness, G. Kovács, K. S. Krughoff, R. H. Lupton, N. B. Lust, L. A. MacArthur, J. Meyers, F. Moolekamp, C. B. Morrison, T. D. Morton, W. O'Mullane, J. K. Parejko, A. A. Plazas, P. A. Price, M. L. Rawls, S. L. Reed, P. Schellart, C. T. Slater, I. Sullivan, J. D. Swinbank, D. Taranu, C. Z. Waters, W. M. Wood-Vasey, An overview of the LSST image processing pipelines. arXiv:1812.03248 [astro-ph.IM] (2019).
17. K. M. Pontoppidan, T. E. Pickering, V. G. Laidler, K. Gilbert, C. D. Sontag, C. Slocum, M. J. Sienkiewicz Jr., C. Hanley, N. M. Earl, L. Pueyo, S. Ravindranath, D. M. Karakla, M. Robberto, A. Noriega-Crespo, E. A. Barker, "Pandeia: a multi-mission exposure time calculator for JWST and WFIRST" in *Observatory Operations: Strategies, Processes, and Systems VI*, A. B. Peck, R. L. Seaman, C. R. Benn, Eds. (SPIE, 2016), vol. 9910, pp. 381–395; https://doi.org/10.1117/12.2231768.
18. H. Seddik, E. Ben Braiek, Efficient noise removing based optimized smart dynamic Gaussian filter. *Int. J. Comput. Appl.* **51**, 1–13 (2012). doi:10.5120/8035-1334
19. Y. Zhu, C. Huang, An improved median filtering algorithm for image noise reduction. *Phys. Procedia* **25**, 609–616 (2012). doi:10.1016/j.phpro.2012.03.133
20. T. Liu, Y. Quan, Y. Su, Y. Guo, S. Liu, H. Ji, Q. Hao, Y. Gao, Y. Liu, Y. Wang, W. Sun, M. Ding, Astronomical image denoising by self-supervised deep learning and restoration processes. *Nat. Astron.* **9**, 608–615 (2025). doi:10.1038/s41550-025-02484-z
21. Y. Zhang, B. Nord, A. Pagul, M. Lepori, Noise2Astro: Astronomical Image Denoising with Self-supervised Neural Networks. *Res. Notes AAS* **6**, 187 (2022). doi:10.3847/2515-5172/ac9140
22. A. Vojtekova, M. Lieu, I. Valtchanov, B. Altieri, L. Old, Q. Chen, F. Hroch, Learning to denoise astronomical images with U-nets. *Mon. Not. R. Astron. Soc.* **503**, 3204–3215 (2021). doi:10.1093/mnras/staa3567
23. J. Qi, M. Chen, Z. Wu, C. Su, X. Yao, C. Mei, "An improved U-Net model for astronomical images denoising" in *2022 China Automation Congress (CAC)* (IEEE, 2022), vol. 2022, pp. 1901–1905.
24. K. Zhang, W. Zuo, Y. Chen, D. Meng, L. Zhang, Beyond a Gaussian denoiser: residual learning of deep CNN for image denoising. *IEEE Trans. Image Process.* **26**, 3142–3155 (2017). doi:10.1109/TIP.2017.2662206 Medline
25. B. Mildenhall, J. T. Barron, J. Chen, D. Sharlet, R. Ng, R. Carroll, "Burst denoising with kernel prediction networks" in *Proceedings of the IEEE Conference on Computer Vision and Pattern Recognition* (CVPR, 2018), pp. 2502–2510.
26. C. Godard, K. Matzen, M. Uyttendaele, "Deep burst denoising" in *Proceedings of the European Conference on Computer Vision* (ECCV, 2018), pp. 538–554.
27. T. Huang, S. Li, X. Jia, H. Lu, J. Liu, "Neighbor2Neighbor: Self-supervised denoising from single noisy images" in *Proceedings of the IEEE/CVF Conference on Computer Vision and Pattern Recognition* (CVPR, 2021), pp. 14776–14790.
28. Y. Quan, M. Chen, "Self2Self with dropout: Learning self-supervised denoising from single image" in *Proceedings of the IEEE/CVF Conference on Computer Vision and Pattern Recognition* (CVPR, 2020), pp. 1890–1898.
29. A. Krull, T.-O. Buchholz, F. Jug, "Noise2Void: Learning denoising from single noisy

images" in *Proceedings of the IEEE/CVF Conference on Computer Vision and Pattern Recognition* (CVPR, 2019), pp. 2129–2137.

30. J. Lehtinen, J. Munkberg, J. Hasselgren, S. Laine, T. Karras, M. Aittala, T. Aila, "Noise2Noise: Learning image restoration without clean data" in *Proceedings of the 35th International Conference on Machine Learning* (ICML, 2018), pp. 2965–2974.
31. J. Oppliger, M. M. Denner, J. Küspert, R. Frison, Q. Wang, A. Morawietz, O. Ivashko, A.-C. Dippel, M. V. Zimmermann, I. Biało, L. Martinelli, B. Fauqué, J. Choi, M. Garcia-Fernandez, K.-J. Zhou, N. B. Christensen, T. Kurosawa, N. Momono, M. Oda, F. D. Natterer, M. H. Fischer, T. Neupert, J. Chang, Weak signal extraction enabled by deep neural network denoising of diffraction data. *Nat. Mach. Intell.* **6**, 180–186 (2024). doi:10.1038/s42256-024-00790-1 Medline
32. A. M. Koekemoer, K. Linday, "An investigation of optimal dither strategies for JWST" (Space Telescope Science Institute, 2005); https://www.stsci.edu/files/live/sites/www/files/home/jwst/documentation/technical-documents/_documents/JWST-STScI-000647.pdf.
33. Materials and methods are available as supplementary materials.
34. S. Fujimoto, R. P. Naidu, J. Chisholm, H. Atek, R. Endsley, V. Kokorev, L. J. Furtak, R. Pan, B. Liu, V. Bromm, A. Venditti, E. Visbal, R. Sarmento, A. Weibel, P. A. Oesch, G. Brammer, D. Schaerer, A. Adamo, D. A. Berg, R. Bezanson, R. Bouwens, I. Chemerynska, A. Claeyssens, M. Dessauges-Zavadsky, A. Frebel, D. Korber, I. Labbe, R. Marques-Chaves, J. Matthee, K. B. W. McQuinn, J. B. Muñoz, P. Natarajan, A. Saldana-Lopez, K. A. Suess, M. Volonteri, A. Zitrin, GLIMPSE: An Ultrafaint $\simeq 10^5$ $M_\odot$ Pop III Galaxy Candidate and First Constraints on the Pop III UV Luminosity Function at $z \simeq 6$–7. *Astrophys. J.* **989**, 46 (2025). doi:10.3847/1538-4357/ade9a1
35. K. Dabov, A. Foi, V. Katkovnik, K. Egiazarian, Image denoising by sparse 3-D transform-domain collaborative filtering. *IEEE Trans. Image Process.* **16**, 2080–2095 (2007). doi:10.1109/TIP.2007.901238 Medline
36. M. Maggioni, V. Katkovnik, K. Egiazarian, A. Foi, Nonlocal transform-domain filter for volumetric data denoising and reconstruction. *IEEE Trans. Image Process.* **22**, 119–133 (2013). doi:10.1109/TIP.2012.2210725 Medline
37. S. Waqas Zamir, A. Arora, S. Khan, M. Hayat, F. Shahbaz Khan, M.-H. Yang, "Restormer: Efficient Transformer for High-Resolution Image Restoration" in *Proceedings of the IEEE/CVF Conference on Computer Vision and Pattern Recognition* (CVPR, 2022), pp. 5728–5739.
38. E. Bertin, S. Arnouts, SExtractor: Software for source extraction. *Astron. Astrophys. Suppl. Ser.* **117**, 393–404 (1996). doi:10.1051/aas:1996164
39. F. J. Massey Jr., The Kolmogorov-Smirnov test for goodness of fit. *J. Am. Stat. Assoc.* **46**, 68–78 (1951). doi:10.1080/01621459.1951.10500769
40. C. Impey, G. Bothun, Low surface brightness galaxies. *Annu. Rev. Astron. Astrophys.* **35**, 267–307 (1997). doi:10.1146/annurev.astro.35.1.267
41. M. G. Lee, J. H. Bae, I. S. Jang, Detection of intracluster globular clusters in the first JWST images of the gravitational lens cluster SMACS J0723.3–7327 at $z = 0.39$. *Astrophys. J. Lett.* **940**, L19 (2022). doi:10.3847/2041-8213/ac990b
42. K. A. Suess, J. R. Weaver, S. H. Price, R. Pan, B. Wang 王, R. Bezanson, G. Brammer, S. E. Cutler, I. Labbé, J. Leja, C. C. Williams, K. E. Whitaker, H. Atek, P. Dayal, A. de Graaff, R. Feldmann, M. Franx, Y. Fudamoto, S. Fujimoto, L. J. Furtak, A. D. Goulding, J. E. Greene, G. Khullar, V. Kokorev, M. Kriek, B. Lorenz, D. Marchesini, M. V. Maseda, J. Matthee, T. B. Miller, I. Mitsuhashi, L. A. Mowla, A. Muzzin, R. P. Naidu, T. Nanayakkara, E. J. Nelson, P. A. Oesch, D. J. Setton, H. Shipley, R. Smit, J. S. Spilker, P. van Dokkum, A. Zitrin, Medium bands, mega science: A JWST/NIRCam medium-band imaging survey of A2744. *Astrophys. J.* **976**, 101 (2024). doi:10.3847/1538-4357/ad75fe
43. Y. Wu, Z. Cai, F. Sun, F. Bian, X. Lin, Z. Li, M. Li, F. E. Bauer, E. Egami, X. Fan, J. González-López, J. Li, F. Wang, J. Yang, S. Zhang, S. Zou, The identification of a dusty multiarm spiral galaxy at $z = 3.06$ with JWST and ALMA. *Astrophys. J. Lett.* **942**, L1 (2023). doi:10.3847/2041-8213/aca652
44. W. Wang, S. Cantalupo, A. Pensabene, M. Galbiati, A. Travascio, C. C. Steidel, M. V. Maseda, G. Pezzulli, S. de Beer, M. Fossati, M. Fumagalli, S. G. Gallego, T. Lazeyras, R. Mackenzie, J. Matthee, T. Nanayakkara, G. Quadri, A giant disk galaxy two billion years after the Big Bang. *Nat. Astron.* **9**, 710–719 (2025). doi:10.1038/s41550-025-02500-2 Medline
45. Z. Wang, A. C. Bovik, H. R. Sheikh, E. P. Simoncelli, Image quality assessment: From error visibility to structural similarity. *IEEE Trans. Image Process.* **13**, 600–612 (2004). doi:10.1109/TIP.2003.819861 Medline
46. Y. Fudamoto, F. Sun, J. M. Diego, L. Dai, M. Oguri, A. Zitrin, E. Zackrisson, M. Jauzac, D. J. Lagattuta, E. Egami, E. Iani, R. A. Windhorst, K. T. Abe, F. E. Bauer, F. Bian, R. Bhatawdekar, T. J. Broadhurst, Z. Cai, C.-C. Chen, W. Chen, S. H. Cohen, C. J. Conselice, D. Espada, N. Foo, B. L. Frye, S. Fujimoto, L. J. Furtak, M. Golubchik, T. Y.-Y. Hsiao, J.-B. Jolly, H. Kawai, P. L. Kelly, A. M. Koekemoer, K. Kohno, V. Kokorev, M. Li, Z. Li, X. Lin, G. E. Magdis, A. K. Meena, A. Niemiec, A. Nabizadeh, J. Richard, C. L. Steinhardt, Y. Wu, Y. Zhu, S. Zou, Identification of more than 40 gravitationally magnified stars in a galaxy at redshift 0.725. *Nat. Astron.* **9**, 428–437 (2025). doi:10.1038/s41550-024-02432-3
47. J. Walawender, M. Wung, M. Fabricius, I. Tanaka, N. Arimoto, D. Cook, B. Elms, Y. Hashiba, Y.-S. Hu, I. Iwata, T. Nishimura, K. Omata, N. Takato, S.-Y. Wang, M. Weber, "The nuMOIRCS project: Detector upgrade overview and early commissioning results" in *Ground-Based and Airborne Instrumentation for Astronomy VI*, C. J. Evans, L. Simard, H. Takami, Eds. (SPIE, 2016), vol. 9908, p. 99082G; https://doi.org/10.1117/12.2231812.
48. M. Fabricius, J. Walawender, N. Arimoto, D. Cook, B. Elms, Y. Hashiba, T. Hattori, Y.-S. Hu, I. Iwata, T. Nishimura, K. Omata, P. Tait, N. Takato, I. Tanaka, S.-Y. Wang, M. Weber, M. Wung, "Detector upgrade of Subaru's Multi-object Infrared Camera and Spectrograph (MOIRCS)" in *Ground-Based and Airborne Instrumentation for Astronomy VI*, C. J. Evans, L. Simard, H. Takami, Eds. (SPIE, 2016), vol. 9908, p. 990828; https://doi.org/10.1117/12.2231417.
49. S. Zhang, Z. Cai, D. Xu, R. Shimakawa, F. Arrigoni Battaia, J. X. Prochaska, R. Cen, Z. Zheng, Y. Wu, Q. Li, L. Dou, J. Wu, A. Zabludoff, X. Fan, Y. Ai, E. G. Golden-Marx, M. Li, Y. Lu, X. Ma, S. Wang, R. Wang, F. Yuan, Inspiraling streams of enriched gas observed around a massive galaxy 11 billion years ago. *Science* **380**, 494–498 (2023). doi:10.1126/science.abj9192 Medline
50. D. J. Eisenstein, B. D. Johnson, B. Robertson, S. Tacchella, K. Hainline, P. Jakobsen, R. Maiolino, N. Bonaventura, A. J. Bunker, A. J. Cameron, P. A. Cargile, E. Curtis-Lake, R. Hausen, D. Puskás, M. Rieke, F. Sun, C. N. A. Willmer, C. Willott, S. Alberts, S. Arribas, W. M. Baker, S. Baum, R. Bhatawdekar, S. Carniani, S. Charlot, Z. Chen, J. Chevallard, M. Curti, C. DeCoursey, F. D'Eugenio, A. de Graaff, E. Egami, J. M. Helton, Z. Ji, G. C. Jones, N. Kumari, N. Lützgendorf, I. Laseter, T. J. Looser, J. Lyu, M. V. Maseda, E. Nelson, E. Parlanti, B. J. Rauscher, T. Rawle, G. Rieke, H.-W. Rix, W. Rujopakarn, L. Sandles, A. Saxena, J. Scholtz, K. Sharpe, I. Shivaei, C. Simmonds, R. Smit, M. W. Topping, H. Übler, G. Venturi, C. C. Williams, J. Witstok, C. Woodrum, The JADES origins field: A new JWST deep field in the JADES second NIRCam data release. *Astrophys. J. Suppl. Ser.* **281**, 50 (2025). doi:10.3847/1538-4365/ae1137
51. A. J. Bunker, A. J. Cameron, E. Curtis-Lake, P. Jakobsen, S. Carniani, M. Curti, J. Witstok, R. Maiolino, F. D'Eugenio, T. J. Looser, C. Willott, N. Bonaventura, K. Hainline, H. Übler, C. N. A. Willmer, A. Saxena, R. Smit, S. Alberts, S. Arribas, W. M. Baker, S. Baum, R. Bhatawdekar, R. A. A. Bowler, K. Boyett, S. Charlot, Z. Chen, J. Chevallard, C. Circosta, C. DeCoursey, A. de Graaff, E. Egami, D. J. Eisenstein, R. Endsley, P. Ferruit, G. Giardino, R. Hausen, J. M. Helton, R. E. Hviding, Z. Ji, B. D. Johnson, G. C. Jones, N. Kumari, I. Laseter, N. Lützgendorf, M. V. Maseda, E. Nelson, E. Parlanti, M. Perna, B. J. Rauscher, T. Rawle, H.-W. Rix, M. Rieke, B. Robertson, B. Rodríguez Del Pino, L. Sandles, J. Scholtz, K. Sharpe, M. Skarbinski, D. P. Stark, F. Sun, S. Tacchella, M. W. Topping, N. C. Villanueva, I. E. B. Wallace, C. C. Williams, C. Woodrum, JADES NIRSpec initial data release for the *Hubble* Ultra Deep Field. *Astron. Astrophys.* **690**, A288 (2024). doi:10.1051/0004-6361/202347094
52. B. Robertson, B. D. Johnson, S. Tacchella, D. J. Eisenstein, K. Hainline, S. Arribas, W. M. Baker, A. J. Bunker, S. Carniani, P. A. Cargile, C. Carreira, S. Charlot, J. Chevallard, M. Curti, E. Curtis-Lake, F. D'Eugenio, E. Egami, R. Hausen, J. M. Helton, P. Jakobsen, Z. Ji, G. C. Jones, R. Maiolino, M. V. Maseda, E. Nelson, P. G. Pérez-González, D. Puskás, M. Rieke, R. Smit, F. Sun, H. Übler, L. Whitler, C. C. Williams, C. N. A. Willmer, C. Willott, J. Witstok, Earliest galaxies in the JADES origins field: Luminosity function and cosmic star formation rate density 300 Myr after the Big Bang. *Astrophys. J.* **970**, 31 (2024). doi:10.3847/1538-4357/ad463d
53. L. Whitler, D. P. Stark, M. W. Topping, B. Robertson, M. Rieke, K. N. Hainline, R. Endsley, Z. Chen, W. M. Baker, R. Bhatawdekar, A. J. Bunker, S. Carniani, S. Charlot, J. Chevallard, E. Curtis-Lake, E. Egami, D. J. Eisenstein, J. M. Helton, Z. Ji, B. D. Johnson, P. G. Pérez-González, P. Rinaldi, S. Tacchella, C. C. Williams, C. N. A. Willmer, C. Willott, J. Witstok, The $z \gtrsim 9$ galaxy UV luminosity function from the

JWST advanced deep extragalactic survey: Insights into early galaxy evolution and reionization. *Astrophys. J.* **992**, 63 (2025). doi:10.3847/1538-4357/adfddc

54. C. C. Steidel, K. L. Adelberger, M. Giavalisco, M. Dickinson, Lyman-Break galaxies at $z \geq 4$ and the evolution of the ultraviolet luminosity density at high redshift. *Astrophys. J.* **519**, 1–17 (1999). doi:10.1086/307363
55. Y. Harikane, A. K. Inoue, R. S. Ellis, M. Ouchi, Y. Nakazato, N. Yoshida, Y. Ono, F. Sun, R. A. Sato, G. Ferrami, S. Fujimoto, N. Kashikawa, D. J. McLeod, P. G. Pérez-González, M. Sawicki, Y. Sugahara, Y. Xu, S. Yamanaka, A. C. Carnall, F. Cullen, J. S. Dunlop, E. Egami, N. Grogin, Y. Isobe, A. M. Koekemoer, N. Laporte, C.-H. Lee, D. Magee, H. Matsuo, Y. Matsuoka, K. Mawatari, K. Nakajima, M. Nakane, Y. Tamura, H. Umeda, H. Yanagisawa, JWST, ALMA, and Keck spectroscopic constraints on the UV luminosity functions at $z \sim 7-14$: Clumpiness and compactness of the brightest galaxies in the early universe. *Astrophys. J.* **980**, 138 (2025). doi:10.3847/1538-4357/ad9b2c
56. P. Arrabal Haro, M. Dickinson, S. L. Finkelstein, J. S. Kartaltepe, C. T. Donnan, D. Burgarella, A. C. Carnall, F. Cullen, J. S. Dunlop, V. Fernández, S. Fujimoto, I. Jung, M. Krips, R. L. Larson, C. Papovich, P. G. Pérez-González, R. O. Amorín, M. B. Bagley, V. Buat, C. M. Casey, K. Chworowsky, S. H. Cohen, H. C. Ferguson, M. Giavalisco, M. Huertas-Company, T. A. Hutchison, D. D. Kocevski, A. M. Koekemoer, R. A. Lucas, D. J. McLeod, R. J. McLure, N. Pirzkal, L.-M. Seillé, J. R. Trump, B. J. Weiner, S. M. Wilkins, J. A. Zavala, Confirmation and refutation of very luminous galaxies in the early Universe. *Nature* **622**, 707–711 (2023). doi:10.1038/s41586-023-06521-7 Medline
57. G. Sun, C.-A. Faucher-Giguère, C. C. Hayward, X. Shen, A. Wetzel, R. K. Cochrane, Bursty star formation naturally explains the abundance of bright galaxies at cosmic dawn. *Astrophys. J. Lett.* **955**, L35 (2023). doi:10.3847/2041-8213/acf85a
58. A. Dekel, K. C. Sarkar, Y. Birnboim, N. Mandelker, Z. Li, Efficient formation of massive galaxies at cosmic dawn by feedback-free starbursts. *Mon. Not. R. Astron. Soc.* **523**, 3201–3218 (2023). doi:10.1093/mnras/stad1557
59. C. C. Williams, S. Tacchella, M. V. Maseda, B. E. Robertson, B. D. Johnson, C. J. Willott, D. J. Eisenstein, C. N. A. Willmer, Z. Ji, K. N. Hainline, J. M. Helton, S. Alberts, S. Baum, R. Bhatawdekar, K. Boyett, A. J. Bunker, S. Carniani, S. Charlot, J. Chevallard, E. Curtis-Lake, A. de Graaff, E. Egami, M. Franx, N. Kumari, R. Maiolino, E. J. Nelson, M. J. Rieke, L. Sandles, I. Shivaei, C. Simmonds, R. Smit, K. A. Suess, F. Sun, H. Übler, J. Witstok, JEMS: A deep medium-band imaging survey in the hubble ultra deep field with JWST NIRCam and NIRISS. *Astrophys. J. Suppl. Ser.* **268**, 64 (2023). doi:10.3847/1538-4365/acf130
60. H. Bushouse, J. Eisenhamer, N. Dencheva, J. Davies, P. Greenfield, J. Morrison, P. Hodge, B. Simon, D. Grumm, M. Droettboom, E. Slavich, M. Sosey, T. Pauly, T. Miller, R. Jedrzejewski, W. Hack, D. Davis, S. Crawford, D. Law, K. Gordon, M. Regan, M. Cara, K. MacDonald, L. Bradley, C. Shanahan, W. Jamieson, M. Teodoro, T. Williams, JWST Calibration Pipeline. Zenodo (2023); https://doi.org/10.5281/zenodo.7325378.
61. J. Rigby, M. Perrin, M. McElwain, R. Kimble, S. Friedman, M. Lallo, R. Doyon, L. Feinberg, P. Ferruit, A. Glasse, M. Rieke, G. Rieke, G. Wright, C. Willott, K. Colon, S. Milam, S. Neff, C. Stark, J. Valenti, J. Abell, F. Abney, Y. Abul-Huda, D. Scott Acton, E. Adams, D. Adler, J. Aguilar, N. Ahmed, L. Albert, S. Alberts, D. Aldridge, M. Allen, M. Altenburg, J. Álvarez-Márquez, C. Alves de Oliveira, G. Andersen, H. Anderson, S. Anderson, I. Argyriou, A. Armstrong, S. Arribas, E. Artigau, A. Arvai, C. Atkinson, G. Bacon, T. Bair, K. Banks, J. Barrientes, B. Barringer, P. Bartosik, W. Bast, P. Baudoz, T. Beatty, K. Bechtold, T. Beck, E. Bergeron, M. Bergkoetter, R. Bhatawdekar, S. Birkmann, R. Blazek, C. Blome, A. Boccaletti, T. Böker, J. Boia, N. Bonaventura, N. Bond, K. Bosley, R. Boucarut, M. Bourque, J. Bouwman, G. Bower, C. Bowers, M. Boyer, L. Bradley, G. Brady, H. Braun, D. Breda, P. Bresnahan, S. Bright, C. Britt, A. Bromenschenkel, B. Brooks, K. Brooks, B. Brown, M. Brown, P. Brown, A. Bunker, M. Burger, H. Bushouse, S. Cale, A. Cameron, P. Cameron, A. Canipe, J. Caplinger, F. Caputo, M. Cara, L. Carey, S. Carniani, M. Carrasquilla, M. Carruthers, M. Case, R. Catherine, D. Chance, G. Chapman, S. Charlot, B. Charlow, P. Chayer, B. Chen, B. Cherinka, S. Chichester, Z. Chilton, T. Chonis, M. Clampin, C. Clark, K. Clark, D. Coe, B. Coleman, B. Comber, T. Comeau, D. Connolly, J. Cooper, R. Cooper, E. Coppock, M. Correnti, C. Cossou, A. Coulais, L. Coyle, M. Cracraft, M. Curti, S. Cuturic, K. Davis, M. Davis, B. Dean, A. DeLisa, W. deMeester, N. Dencheva, N. Dencheva, J. DePasquale, J. Deschenes, Ö. Hunor Detre, R. Diaz, D. Dicken, A. DiFelice, M. Dillman, W. Dixon, J. Doggett, T. Donaldson, R. Douglas, K. DuPrie, J. Dupuis, J. Durning, N. Easmin, W. Eck, C. Edeani, E. Egami, R. Ehrenwinkler, J. Eisenhamer, M. Eisenhower, M. Elie, J. Elliott, K. Elliott, T. Ellis, M. Engesser, N. Espinoza, O. Etienne, M. Etxaluze, P. Falini, M. Feeney, M. Ferry, J. Filippazzo, B. Fincham, M. Fix, N. Flagey, M. Florian, J. Flynn, E. Fontanella, T. Ford, P. Forshay, O. Fox, D. Franz, H. Fu, A. Fullerton, S. Galkin, A. Galyer, M. García Marín, J. P. Gardner, L. Gardner, D. Garland, B. Garrett, D. Gasman, A. Gaspar, D. Gaudreau, P. Gauthier, V. Geers, P. Geithner, M. Gennaro, G. Giardino, J. Girard, M. Giuliano, K. Glassmire, A. Glauser, S. Glazer, J. Godfrey, D. Golimowski, D. Gollnitz, F. Gong, S. Gonzaga, M. Gordon, K. Gordon, P. Goudfrooij, T. Greene, M. Greenhouse, S. Grimaldi, A. Groebner, T. Grundy, P. Guillard, I. Gutman, K. Q. Ha, P. Haderlein, A. Hagedorn, K. Hainline, C. Haley, M. Hami, F. Hamilton, H. Hammel, C. Hansen, T. Harkins, M. Harr, J. Hart, Q. Hart, G. Hartig, R. Hashimoto, S. Haskins, W. Hathaway, K. Havey, B. Hayden, K. Hecht, C. Heller-Boyer, C. Henriques, A. Henry, K. Hermann, S. Hernandez, B. Hesman, B. Hicks, B. Hilbert, D. Hines, M. Hoffman, S. Holfeltz, B. J. Holler, J. Hoppa, K. Hott, J. M. Howard, R. Howard, A. Hunter, D. Hunter, B. Hurst, B. Husemann, L. Hustak, L. Ilinca Ignat, G. Illingworth, S. Irish, W. Jackson, A. Jahromi, P. Jakobsen, L. A. James, B. James, W. Januszewski, A. Jenkins, H. Jirdeh, P. Johnson, T. Johnson, V. Jones, R. Jones, D. Jones, O. Jones, I. Jordan, M. Jordan, S. Jurczyk, A. Jurling, C. Kaleida, P. Kalmanson, J. Kammerer, H. Kang, S.-H. Kao, D. Karakla, P. Kavanagh, D. Kelly, S. Kendrew, H. Kennedy, D. Kenny, R. Keski-kuha, C. Keyes, R. Kidwell, W. Kinzel, J. Kirk, M. Kirkpatrick, D. Kirshenblat, P. Klaassen, B. Knapp, J. Scott Knight, P. Knollenberg, R. Koehler, A. Koekemoer, A. Kovacs, T. Kulp, N. Kumari, M. Kyprianou, S. La Massa, A. Labador, A. Labiano, P.-O. Lagage, C.-P. Lajoie, M. Lallo, M. Lam, T. Lamb, S. Lambros, R. Lampenfield, J. Langston, K. Larson, D. Law, J. Lawrence, D. Lee, J. Leisenring, K. Lepo, M. Leveille, N. Levenson, M. Levine, Z. Levy, D. Lewis, H. Lewis, M. Libralato, P. Lightsey, M. Link, L. Liu, A. Lo, A. Lockwood, R. Logue, C. Long, D. Long, C. Loomis, M. Lopez-Caniego, J. Lorenzo Alvarez, J. Love-Pruitt, A. Lucy, N. Luetzgendorf, P. Maghami, R. Maiolino, M. Major, S. Malla, E. Malumuth, E. Manjavacas, C. Mannfolk, A. Marrione, A. Marston, A. Martel, M. Maschmann, G. Masci, M. Masciarelli, M. Maszkiewicz, J. Mather, K. McKenzie, B. McLean, M. McMaster, K. Melbourne, M. Meléndez, M. Menzel, K. Merz, M. Meyett, L. Meza, C. Miskey, K. Misselt, C. Moller, J. Morrison, E. Morse, H. Moseley, G. Mosier, M. Mountain, J. Mueckay, M. Mueller, S. Mullally, J. Murphy, K. Murray, C. Murray, D. Mustelier, J. Muzerolle, M. Mycroft, R. Myers, K. Myrick, S. Nanavati, E. Nance, O. Nayak, B. Naylor, E. Nelan, B. Nickson, A. Nielson, M. Nieto-Santisteban, N. Nikolov, A. Noriega-Crespo, B. O'Shaughnessy, B. O'Sullivan, W. Ochs, P. Ogle, B. Oleszczuk, J. Olmsted, S. Osborne, R. Ottens, B. Owens, C. Pacifici, A. Pagan, J. Page, S. Park, K. Parrish, P. Patapis, L. Paul, T. Pauly, C. Pavlovsky, A. Pedder, M. Peek, M. Pena-Guerrero, K. Penanen, Y. Perez, M. Perna, B. Perriello, K. Phillips, M. Pietraszkiewicz, J.-P. Pinaud, N. Pirzkal, J. Pitman, A. Piwowar, V. Platais, D. Player, R. Plesha, J. Pollizi, E. Polster, K. Pontoppidan, B. Porterfield, C. Proffitt, L. Pueyo, C. Pulliam, B. Quirt, I. Quispe Neira, R. Ramos Alarcon, L. Ramsay, G. Rapp, R. Rapp, B. Rauscher, S. Ravindranath, T. Rawle, M. Regan, T. A. Reichard, C. Reis, M. E. Ressler, A. Rest, P. Reynolds, T. Rhue, K. Richon, E. Rickman, M. Ridgaway, C. Ritchie, H.-W. Rix, M. Robberto, G. Robinson, M. Robinson, O. Robinson, F. Rock, D. Rodriguez, B. Rodriguez Del Pino, T. Roellig, S. Rohrbach, A. Roman, F. Romelfanger, P. Rose, A. Roteliuk, M. Roth, B. Rothwell, N. Rowlands, A. Roy, P. Royer, P. Royle, C. Rui, P. Rumler, J. Runnels, M. Russ, Z. Rustamkulov, G. Ryden, H. Ryer, M. Sabata, D. Sabatke, E. Sabbi, B. Samuelson, B. Sapp, B. Sappington, B. Sargent, A. Sauer, S. Scheithauer, E. Schlawin, J. Schlitz, T. Schmitz, A. Schneider, J. Schreiber, V. Schulze, R. Schwab, J. Scott, K. Sembach, C. Shanahan, B. Shaughnessy, R. Shaw, N. Shawger, C. Shay, E. Sheehan, S. Shen, A. Sherman, B. Shiao, H.-Y. Shih, I. Shivaei, M. Sienkiewicz, D. Sing, M. Sirianni, A. Sivaramakrishnan, J. Skipper, G. C. Sloan, C. Slocum, S. Slowinski, E. Smith, E. Smith, D. Smith, C. Smith, G. Snyder, W. Soh, S. Tony Sohn, C. Soto, R. Spencer, S. Stallcup, J. Stansberry, C. Starr, E. Starr, A. Stewart, M. Stiavelli, A. Straughn, D. Strickland, J. Stys, F. Summers, F. Sun, B. Sunnquist, D. Swade, M. Swam, R. Swaters, R. Swoish, J. M. Taylor, R. Taylor, M. Te Plate, M. Tea, K. Teague, R. Telfer, T. Temim, D. Thatte, C. Thompson, L. Thompson, S. Thomson, T. Tikkanen, W. Tippet, C. Todd, S. Toolan, H. Tran, E. Trejo, J. Truong, C. Tsukamoto, S. Tustain, H. Tyra, L. Ubeda, K. Underwood, M. Uzzo, J. Van Campen, T. Vandal, B. Vandenbussche, B. Vila, K. Volk, G. Wahlgren, M. Waldman, C. Walker, M. Wander, C. Warfield, G. Warner, M. Wasiak, M. Watkins, A. Weaver, M. Weilert, N. Weiser, B. Weiss, S. Weissman, A.

Welty, G. West, L. Wheate, E. Wheatley, T. Wheeler, R. White, K. Whiteaker, P. Whitehouse, J. Whiteleather, W. Whitman, C. Williams, C. Willmer, S. Willoughby, A. Wilson, G. Wirth, E. Wislowski, E. Wolf, D. Wolfe, S. Wolff, B. Workman, R. Wright, C. Wu, R. Wu, K. Wymer, K. Yates, C. Yeager, J. Yeates, E. Yerger, J. Yoon, A. Young, S. Yu, D. Zak, P. Zeidler, J. Zhou, T. Zielinski, C. Zincke, S. Zonak, The science performance of JWST as characterized in commissioning. *Publ. Astron. Soc. Pac.* **135**, 048001 (2023). doi:10.1088/1538-3873/acb293

62. M. B. Bagley, S. L. Finkelstein, A. M. Koekemoer, H. C. Ferguson, P. Arrabal Haro, M. Dickinson, J. S. Kartaltepe, C. Papovich, P. G. Pérez-González, N. Pirzkal, R. S. Somerville, C. N. A. Willmer, G. Yang, L. Y. A. Yung, A. Fontana, A. Grazian, N. A. Grogin, M. Hirschmann, L. J. Kewley, A. Kirkpatrick, D. D. Kocevski, J. M. Lotz, A. Medrano, A. M. Morales, L. Pentericci, S. Ravindranath, J. R. Trump, S. M. Wilkins, A. Calabrò, M. C. Cooper, L. Costantin, A. de la Vega, B. Hilbert, T. A. Hutchison, R. L. Larson, R. A. Lucas, E. J. McGrath, R. Ryan, X. Wang, S. Wuyts, CEERS epoch 1 NIRCam imaging: Reduction methods and simulations enabling early JWST science results. *Astrophys. J. Lett.* **946**, L12 (2023). doi:10.3847/2041-8213/acbb08
63. A. Dey, D. J. Schlegel, D. Lang, R. Blum, K. Burleigh, X. Fan, J. R. Findlay, D. Finkbeiner, D. Herrera, S. Juneau, M. Landriau, M. Levi, I. McGreer, A. Meisner, A. D. Myers, J. Moustakas, P. Nugent, A. Patej, E. F. Schlafly, A. R. Walker, F. Valdes, B. A. Weaver, C. Yèche, H. Zou, X. Zhou, B. Abareshi, T. M. C. Abbott, B. Abolfathi, C. Aguilera, S. Alam, L. Allen, A. Alvarez, J. Annis, B. Ansarinejad, M. Aubert, J. Beechert, E. F. Bell, S. Y. BenZvi, F. Beutler, R. M. Bielby, A. S. Bolton, C. Briceño, E. J. Buckley-Geer, K. Butler, A. Calamida, R. G. Carlberg, P. Carter, R. Casas, F. J. Castander, Y. Choi, J. Comparat, E. Cukanovaite, T. Delubac, K. DeVries, S. Dey, G. Dhungana, M. Dickinson, Z. Ding, J. B. Donaldson, Y. Duan, C. J. Duckworth, S. Eftekharzadeh, D. J. Eisenstein, T. Etourneau, P. A. Fagrelius, J. Farihi, M. Fitzpatrick, A. Font-Ribera, L. Fulmer, B. T. Gänsicke, E. Gaztanaga, K. George, D. W. Gerdes, S. G. A Gontcho, C. Gorgoni, G. Green, J. Guy, D. Harmer, M. Hernandez, K. Honscheid, L. W. Huang, D. J. James, B. T. Jannuzi, L. Jiang, R. Joyce, A. Karcher, S. Karkar, R. Kehoe, J.-P. Kneib, A. Kueter-Young, T.-W. Lan, T. R. Lauer, L. L. Guillou, A. L. Van Suu, J. H. Lee, M. Lesser, L. P. Levasseur, T. S. Li, J. L. Mann, R. Marshall, C. E. Martínez-Vázquez, P. Martini, H. du Mas des Bourboux, S. McManus, T. G. Meier, B. Ménard, N. Metcalfe, A. Muñoz-Gutiérrez, J. Najita, K. Napier, G. Narayan, J. A. Newman, J. Nie, B. Nord, D. J. Norman, K. A. G. Olsen, A. Paat, N. Palanque-Delabrouille, X. Peng, C. L. Poppett, M. R. Poremba, A. Prakash, D. Rabinowitz, A. Raichoor, M. Rezaie, A. N. Robertson, N. A. Roe, A. J. Ross, N. P. Ross, G. Rudnick, S. Gaines, A. Saha, F. J. Sánchez, E. Savary, H. Schweiker, A. Scott, H.-J. Seo, H. Shan, D. R. Silva, Z. Slepian, C. Soto, D. Sprayberry, R. Staten, C. M. Stillman, R. J. Stupak, D. L. Summers, S. S. Tie, H. Tirado, M. Vargas-Magaña, A. K. Vivas, R. H. Wechsler, D. Williams, J. Yang, Q. Yang, T. Yapici, D. Zaritsky, A. Zenteno, K. Zhang, T. Zhang, R. Zhou, Z. Zhou, Overview of the DESI legacy imaging surveys. *Astron. J.* **157**, 168 (2019). doi:10.3847/1538-3881/ab089d
64. M. D. Perrin, A. Sivaramakrishnan, C.-P. Lajoie, E. Elliott, L. Pueyo, S. Ravindranath, L. Albert, "Updated point spread function simulations for JWST with WebbPSF" in *Space Telescopes and Instrumentation 2014: Optical, Infrared, and Millimeter Wave*, J. M. Oschmann Jr., M. Clampin, G. G. Fazio, H. A. MacEwen, Eds. (SPIE, 2014), vol. 9143, pp. 91433X; https://doi.org/10.1117/12.2056689.
65. A. A. Taha, A. Hanbury, Metrics for evaluating 3D medical image segmentation: Analysis, selection, and tool. *BMC Med. Imaging* **15**, 29 (2015). doi:10.1186/s12880-015-0068-x Medline
66. W. E. Harris, J. S. Speagle, Photometric completeness modelled with neural networks. *Astron. J.* **168**, 38 (2024). doi:10.3847/1538-3881/ad4a76
67. E. Bertin, "Automated morphometry with SExtractor and PSFEx" in *Astronomical Data Analysis Software and Systems XX*, I. N. Evans, A. Accomazzi, D. J. Mink, A. H. Rots, Eds. (ASP, 2011), p. 435.
68. R. G. Kron, Photometry of a complete sample of faint galaxies. *Astrophys. J. Suppl. Ser.* **43**, 305–325 (1980). doi:10.1086/190669
69. G. B. Brammer, P. G. van Dokkum, P. Coppi, EAZY: A fast, public photometric redshift code. *Astrophys. J.* **686**, 1503–1513 (2008). doi:10.1086/591786
70. K. N. Hainline, B. D. Johnson, B. Robertson, S. Tacchella, J. M. Helton, F. Sun, D. J. Eisenstein, C. Simmonds, M. W. Topping, L. Whitler, C. N. A. Willmer, M. Rieke, K. A. Suess, R. E. Hviding, A. J. Cameron, S. Alberts, W. M. Baker, S. Baum, R. Bhatawdekar, N. Bonaventura, K. Boyett, A. J. Bunker, S. Carniani, S. Charlot, J. Chevallard, Z. Chen, M. Curti, E. Curtis-Lake, F. D'Eugenio, E. Egami, R. Endsley, R. Hausen, Z. Ji, T. J. Looser, J. Lyu, R. Maiolino, E. Nelson, D. Puskás, T. Rawle, L. Sandles, A. Saxena, R. Smit, D. P. Stark, C. C. Williams, C. Willott, J. Witstok, The cosmos in its infancy: JADES galaxy candidates at $z > 8$ in GOODS-S and GOODS-N. *Astrophys. J.* **964**, 71 (2024). doi:10.3847/1538-4357/ad1ee4
71. J. Chevallard, S. Charlot, Modelling and interpreting spectral energy distributions of galaxies with BEAGLE. *Mon. Not. R. Astron. Soc.* **462**, 1415–1443 (2016). doi:10.1093/mnras/stw1756
72. M. Schmidt, Space distribution and luminosity functions of quasi-stellar radio sources. *Astrophys. J.* **151**, 393 (1968). doi:10.1086/149446
73. P. Schechter, An analytic expression for the luminosity function for galaxies. *Astrophys. J.* **203**, 297 (1976). doi:10.1086/154079
74. R. J. Bouwens, P. A. Oesch, M. Stefanon, G. Illingworth, I. Labbé, N. Reddy, H. Atek, M. Montes, R. Naidu, T. Nanayakkara, E. Nelson, S. Wilkins, New determinations of the UV luminosity functions from $z \sim 9$ to 2 show a remarkable consistency with halo growth and a constant star formation efficiency. *Astron. J.* **162**, 47 (2021). doi:10.3847/1538-3881/abf83e
75. Y. Harikane, M. Ouchi, M. Oguri, Y. Ono, K. Nakajima, Y. Isobe, H. Umeda, K. Mawatari, Y. Zhang, A comprehensive study of galaxies at $z \sim 9-16$ found in the early JWST data: Ultraviolet luminosity functions and cosmic star formation history at the pre-reionization epoch. *Astrophys. J. Suppl. Ser.* **265**, 5 (2023). doi:10.3847/1538-4365/acaaa9
76. G. C. K. Leung, M. B. Bagley, S. L. Finkelstein, H. C. Ferguson, A. M. Koekemoer, P. G. Pérez-González, A. Morales, D. D. Kocevski, G. Yang 杨, R. S. Somerville, S. M. Wilkins, L. Y. A. Yung, S. Fujimoto, R. L. Larson, C. Papovich, N. Pirzkal, D. A. Berg, J. M. Lotz, M. Castellano, Ó. A. Chávez Ortiz, Y. Cheng, M. Dickinson, M. Giavalisco, N. P. Hathi, T. A. Hutchison, I. Jung, J. S. Kartaltepe, P. Natarajan, B. Rothberg, NGDEEP epoch 1: The faint end of the luminosity function at $z \sim 9-12$ from ultradeep JWST imaging. *Astrophys. J. Lett.* **954**, L46 (2023). doi:10.3847/2041-8213/acf365
77. N. J. Adams, C. J. Conselice, D. Austin, T. Harvey, L. Ferreira, J. Trussler, I. Juodžbalis, Q. Li, R. Windhorst, S. H. Cohen, R. A. Jansen, J. Summers, S. Tompkins, S. P. Driver, A. Robotham, J. C. J. D'Silva, H. Yan, D. Coe, B. Frye, N. A. Grogin, A. M. Koekemoer, M. A. Marshall, N. Pirzkal, R. E. Ryan Jr., W. P. Maksym, M. J. Rutkowski, C. N. A. Willmer, H. B. Hammel, M. Nonino, R. Bhatawdekar, S. M. Wilkins, L. D. Bradley, T. Broadhurst, C. Cheng, H. Dole, N. P. Hathi, A. Zitrin, EPOCHS. II. The ultraviolet luminosity function from $7.5 < z < 13.5$ using 180 arcmin^2 of deep, blank fields from the PEARLS survey and Public JWST data. *Astrophys. J.* **965**, 169 (2024). doi:10.3847/1538-4357/ad2a7b
78. C. T. Donnan, R. J. McLure, J. S. Dunlop, D. J. McLeod, D. Magee, K. Z. Arellano-Córdova, L. Barrufet, R. Begley, R A A. Bowler, A. C. Carnall, F. Cullen, R. S. Ellis, A. Fontana, G. D. Illingworth, N. A. Grogin, M. L. Hamadouche, A. M. Koekemoer, F.-Y. Liu, C. Mason, P. Santini, T. M. Stanton, JWST PRIMER: A new multifield determination of the evolving galaxy UV luminosity function at redshifts $z \simeq 9-15$. *Mon. Not. R. Astron. Soc.* **533**, 3222–3237 (2024). doi:10.1093/mnras/stae2037
79. P. Behroozi, C. Conroy, R. H. Wechsler, A. Hearin, C. C. Williams, B. P. Moster, L. Y. A. Yung, R. S. Somerville, S. Gottlöber, G. Yepes, R. Endsley, The universe at $z > 10$: predictions for JWST from the UNIVERSEMACHINE DR1. *Mon. Not. R. Astron. Soc.* **499**, 5702–5718 (2020). doi:10.1093/mnras/staa3164
80. R. Kannan, E. Garaldi, A. Smith, R. Pakmor, V. Springel, M. Vogelsberger, L. Hernquist, Introducing the THESAN project: Radiation-magnetohydrodynamic simulations of the epoch of reionization. *Mon. Not. R. Astron. Soc.* **511**, 4005–4030 (2022). doi:10.1093/mnras/stab3710
81. L. Y. A. Yung, R. S. Somerville, S. L. Finkelstein, S. M. Wilkins, J. P. Gardner, Are the ultra-high-redshift galaxies at $z > 10$ surprising in the context of standard galaxy formation models? *Mon. Not. R. Astron. Soc.* **527**, 5929–5948 (2023). doi:10.1093/mnras/stad3484
82. Y. Guo, H. Zhang, M. Li, ASTERIS: Deeper detection limits in astronomical imaging using self-supervised spatiotemporal denoising, Zenodo (2025); https://doi.org/10.5281/zenodo.17115038.
83. Y. Guo, H. Zhang, M. Li, ASTERIS: demonstration datasets, Zenodo (2025); https://doi.org/10.5281/zenodo.17105027.
84. M. Li, ASTERIS JWST Data, The Mikulski Archive for Space Telescopes (MAST) (2025); https://dx.doi.org/10.17909/e37z-3919.

85. M. Li, Y. Liang, Y. Guo, H. Zhang, Subaru MOIRCS data used for training and test of ASTERIS, Zenodo (2025); https://doi.org/10.5281/zenodo.18298066.

86. Y. Guo, H. Zhang, M. Li, ASTERIS: pre-trained model for JWST NIRCam and Subaru MOIRCS, Zenodo (2025); https://doi.org/10.5281/zenodo.18358472.

87. H. Bushouse, P. Greenfield, T. Miller, "The JWST calibration reference data system" in *Astronomical Data Analysis Software and Systems XXI*, P. Ballester, Ed. (ASP, 2012), vol. 461, pp. 737–740.

88. R. Suzuki, C. Tokoku, T. Ichikawa, Y. K. Uchimoto, M. Konishi, T. Yoshikawa, I. Tanaka, T. Yamada, K. Omata, T. Nishimura, Multi-Object Infrared Camera and Spectrograph (MOIRCS) for the Subaru Telescope* I. Imaging. *Publ. Astron. Soc. Jpn.* **60**, 1347–1362 (2008). doi:10.1093/pasj/60.6.1347

89. D. Tody, "IRAF in the nineties" in *Astronomical Data Analysis Software and Systems II*, R. J. Hanisch, R. J. V. Brissenden, J. Barnes, Eds. (ASP, 1993), vol. 52, p. 173.

90. I. Tanaka, C. De Breuck, J. D. Kurk, Y. Taniguchi, T. Kodama, Y. Matsuda, C. Packham, A. Zirm, M. Kajisawa, T. Ichikawa, N. Seymour, D. Stern, A. Stockton, B. P. Venemans, J. Vernet, Discovery of an excess of H emitters around 4C 23.56 at $z = 2.48$. *Publ. Astron. Soc. Jpn.* **63**, S415–S435 (2011). doi:10.1093/pasj/63.sp2.S415

91. C. Gabriel, C. Arviset, D. Ponz, E. Solano, E. Bertin, "Automatic astrometric and photometric calibration with SCAMP" in *Astronomical Data Analysis Software and Systems XV*, C. Gabriel, C. Arviset, D. Ponz, E. Solano, Eds. (ASP, 2006), vol. 351, p. 112.

92. E. Bertin, Y. Mellier, M. Radovich, G. Missonnier, P. Didelon, B. Morin, "The TERAPIX Pipeline" in *Astronomical Data Analysis Software and Systems XI*, D. A. Bohlender, D. Durand, T. H. Handley, Eds. (ASP, 2002), vol. 281, p. 228.

93. O. Ronneberger, P. Fischer, T. Brox, "U-Net: Convolutional networks for biomedical image segmentation" in *Medical Image Computing and Computer-Assisted Intervention–MICCAI 2015*, N. Navab, J. Hornegger, W. Wells, A. Frangi, Eds. (Springer, 2015), pp. 234–241; https://doi.org/10.1007/978-3-319-24574-4_28.

94. V. Lempitsky, A. Vedaldi, D. Ulyanov, "Deep image prior" in *Proceedings of the IEEE Conference on Computer Vision and Pattern Recognition* (IEEE, 2018), pp. 9446–9454.

95. A. Paszke, S. Gross, F. Massa, A. Lerer, J. Bradbury, G. Chanan, T. Killeen, Z. Lin, N. Gimelshein, L. Antiga, A. Desmaison, A. Köpf, E. Yang, Z. DeVito, M. Raison, A. Tejani, S. Chilamkurthy, B. Steiner, L. Fang, J. Bai, S. Chintala, PyTorch: An imperative style, high-performance deep learning library. arXiv:1912.01703 [cs.LG] (2019).

96. J. Ansel, E. Yang, H. He, N. Gimelshein, A. Jain, M. Voznesensky, B. Bao, P. Bell, D. Berard, E. Burovski, G. Chauhan, A. Chourdia, W. Constable, A. Desmaison, Z. DeVito, E. Ellison, W. Feng, J. Gong, M. Gschwind, B. Hirsh, S. Huang, K. Kalambarkar, L. Kirsch, M. Lazos, M. Lezcano, Y. Liang, J. Liang, Y. Lu, C. K. Luk, B. Maher, Y. Pan, C. Puhrsch, M. Reso, M. Saroufim, M. Y. Siraichi, H. Suk, S. Zhang, M. Suo, P. Tillet, X. Zhao, E. Wang, K. Zhou, R. Zou, X. Wang, A. Mathews, W. Wen, G. Chanan, P. Wu, S. Chintala, "PyTorch 2: Faster machine learning through dynamic Python bytecode transformation and graph compilation" in *Proceedings of the 29th ACM International Conference on Architectural Support for Programming Languages and Operating Systems* (ASPLOS, 2024), pp. 929–947.

97. G. H. Rieke, Infrared detector arrays for astronomy. *Annu. Rev. Astron. Astrophys.* **45**, 77–115 (2007). doi:10.1146/annurev.astro.44.051905.092436

98. T. Shibuya, M. Ouchi, Y. Harikane, Morphologies of ~190,000 Galaxies at $z = 0$–10 revealed with HST legacy data. I. Size Evolution. *Astrophys. J. Suppl. Ser.* **219**, 15 (2015). doi:10.1088/0067-0049/219/2/15

99. L. Yang, T. Morishita, N. Leethochawalit, M. Castellano, A. Calabrò, T. Treu, A. Bonchi, A. Fontana, C. Mason, E. Merlin, D. Paris, M. Trenti, G. Roberts-Borsani, M. Bradac, E. Vanzella, B. Vulcani, D. Marchesini, X. Ding, T. Nanayakkara, S. Birrer, K. Glazebrook, T. Jones, K. Boyett, P. Santini, V. Strait, X. Wang, Early results from GLASS-JWST. V: The first rest-frame optical size–luminosity relation of galaxies at $z > 7$. *Astrophys. J. Lett.* **938**, L17 (2022). doi:10.3847/2041-8213/ac8803

100. Y. Ono, Y. Harikane, M. Ouchi, H. Yajima, M. Abe, Y. Isobe, T. Shibuya, J. H. Wise, Y. Zhang, K. Nakajima, H. Umeda, Morphologies of galaxies at $z \gtrsim 9$ uncovered by JWST/NIRCam imaging: Cosmic size evolution and an identification of an extremely compact bright galaxy at $z \sim 12$. *Astrophys. J.* **951**, 72 (2023). doi:10.3847/1538-4357/acd44a

101. Y. Ono, Y. Harikane, M. Ouchi, K. Nakajima, Y. Isobe, T. Shibuya, M. Nakane, H. Umeda, Y. Xu, Y. Zhang, Census for the rest-frame optical and UV morphologies of galaxies at $z = 4 - 10$: First phase of inside-out galaxy formation. *Publ. Astron. Soc. Jpn.* **76**, 219–250 (2024). doi:10.1093/pasj/psae004

102. T. Morishita, M. Stiavelli, R.-R. Chary, M. Trenti, P. Bergamini, M. Chiaberge, N. Leethochawalit, G. Roberts-Borsani, X. Shen, T. Treu, Enhanced subkiloparsec-scale star formation: Results from a JWST size analysis of 341 galaxies at $5 < z < 14$. *Astrophys. J.* **963**, 9 (2024). doi:10.3847/1538-4357/ad1404

103. A. K. Inoue, I. Shimizu, I. Iwata, M. Tanaka, An updated analytic model for attenuation by the intergalactic medium. *Mon. Not. R. Astron. Soc.* **442**, 1805–1820 (2014). doi:10.1093/mnras/stu936

104. G. Chabrier, Galactic stellar and substellar initial mass function. *Publ. Astron. Soc. Pac.* **115**, 763–795 (2003). doi:10.1086/376392

105. Y. C. Pei, Interstellar dust from the Milky Way to the Magellanic Clouds. *Astrophys. J.* **395**, 130 (1992). doi:10.1086/171637

106. M. W. Topping, D. P. Stark, R. Endsley, L. Whitler, K. Hainline, B. D. Johnson, B. Robertson, S. Tacchella, Z. Chen, S. Alberts, W. M. Baker, A. J. Bunker, S. Carniani, S. Charlot, J. Chevallard, E. Curtis-Lake, C. DeCoursey, E. Egami, D. J. Eisenstein, Z. Ji, R. Maiolino, C. C. Williams, C. N. A. Willmer, C. Willott, J. Witstok, The UV continuum slopes of early star-forming galaxies in JADES. *Mon. Not. R. Astron. Soc.* **529**, 4087–4103 (2024). doi:10.1093/mnras/stae800

107. J. Sérsic, Influence of the atmospheric and instrumental dispersion on the brightness distribution in a galaxy. *Boletin de la Asociacion Argentina de Astronomia La Plata Argentina* **6**, 41–43 (1963).

108. B. T. P. Rowe, M. Jarvis, R. Mandelbaum, G. M. Bernstein, J. Bosch, M. Simet, J. E. Meyers, T. Kacprzak, R. Nakajima, J. Zuntz, H. Miyatake, J. P. Dietrich, R. Armstrong, P. Melchior, M. S. S. Gill, GalSim: The modular galaxy image simulation toolkit. *Astron. Comput.* **10**, 121–150 (2015). doi:10.1016/j.ascom.2015.02.002

109. M. Trenti, M. Stiavelli, Cosmic variance and its effect on the luminosity function determination in deep high-z Surveys. *Astrophys. J.* **676**, 767–780 (2008). doi:10.1086/528674

ACKNOWLEDGMENTS

We thank Chen Zhu, Peixin Weng and Zuyi Chen for helpful discussions. We acknowledge Rhythm Shimakawa as the principal investigator of the Subaru program S17A-198S, and Ichi Tanaka for assistance with the Subaru MOIRCS data processing. We gratefully acknowledge the NASA/ESA/CSA James Webb Space Telescope mission and its public-access data policy, and particularly thank the investigators of programs 1210, 1963, 3215, 3293, and 4111, whose public data were instrumental in the development and fine-tuning of ASTERIS. This work is based in part on observations made with the NASA/ESA/CSA James Webb Space Telescope. The JWST data were obtained from the Mikulski Archive for Space Telescopes (MAST) at the Space Telescope Science Institute, which is operated by the Association of Universities for Research in Astronomy, Inc., under NASA contract NAS 5-03127 for JWST. This research is based in part on data collected at the Subaru Telescope and obtained from the SMOKA, which are operated by the National Astronomical Observatory of Japan. We are honored and grateful for the opportunity of observing the Universe from Mauna Kea, which has cultural, historical, and natural importance in Hawaii. **Funding:** Q.D. was funded by National Natural Science Foundation of China, grant number 62088102. Z.C. was funded by National Key R&D Program of China, grant number 2023YFA1605600, National Natural Science Foundation of China, grant number 12525303, and Tsinghua University Initiative Scientific Research Program. J.W. was funded by National Natural Science Foundation of China, grant number 62222508 and 62525506. Y.G. was funded by National Natural Science Foundation of China, grant number 62505156, and China Postdoctoral Science Foundation 2024M761675 and 2025T180226. H.Z. was funded by National Natural Science Foundation of China, grant number 62505157. Y.G., J.W., and Q.D. were funded by Beijing Key Laboratory of Cognitive Intelligence. Z.C. and J.W. were funded by New Cornerstone Science Foundation through the XPLORER PRIZE. **Author contributions:** Conceptualization: Y.G., J.W., Z.C. Methodology: Y.G., H.Z., Y.H., S.H. Investigation: Y.G., Z.C., H.Z., M.L., Y.W. JWST data preparation: Z.C., F.Y., M.L., Y.W., H.Z. Subaru data preparation: M.L., H.Z., Y.L., Z.C. Luminosity function: M.L., Z.C., Y.G., H.Z., Y.W., F.Y., X.Lin. Visualization: Y.G., H.Z., M.L. Funding acquisition: Q.D., Z.C., J.W., Y.G., H.Z.

Project administration: Y.G, Z.C., J.W. Supervision: Q.D., Z.C., J.W. Writing – original draft: Y.G., M.L., H.Z. Writing – review and editing: Y.G., H.Z., M.L., J.W., Z.C., Q.D., S.H., Y.L., X.Lin., X.Li. **Competing interests:** The authors declare no competing interests. **Data, code, and materials availability:** The source code for our implementation of ASTERIS in Python is available at https://github.com/freemercury/ASTERIS_THU.git and the version used for this study is archived at Zenodo (*82*). The demonstration data we used are also archived at Zenodo (*83*). The JWST data are available from MAST (*84*) or can be accessed via https://mast.stsci.edu/portal/Mashup/Clients/Mast/Portal.html under program IDs 1210, 1963, 3215, 3293, and 4111. The Subaru data are archived at Zenodo (*85*). The pre-trained ASTERIS models for JWST NIRCam and Subaru MOIRCS are also archived at Zenodo (*86*). No physical materials were generated in this work.

SUPPLEMENTARY MATERIALS

science.org/doi/10.1126/science.ady9404
Materials and Methods
Figs. S1 to S21
Tables S1 to S3
References (*87*–*109*)
Data S1

Submitted 12 May 2025; accepted 28 January 2026
Published online 19 February 2026
10.1126/science.ady9404

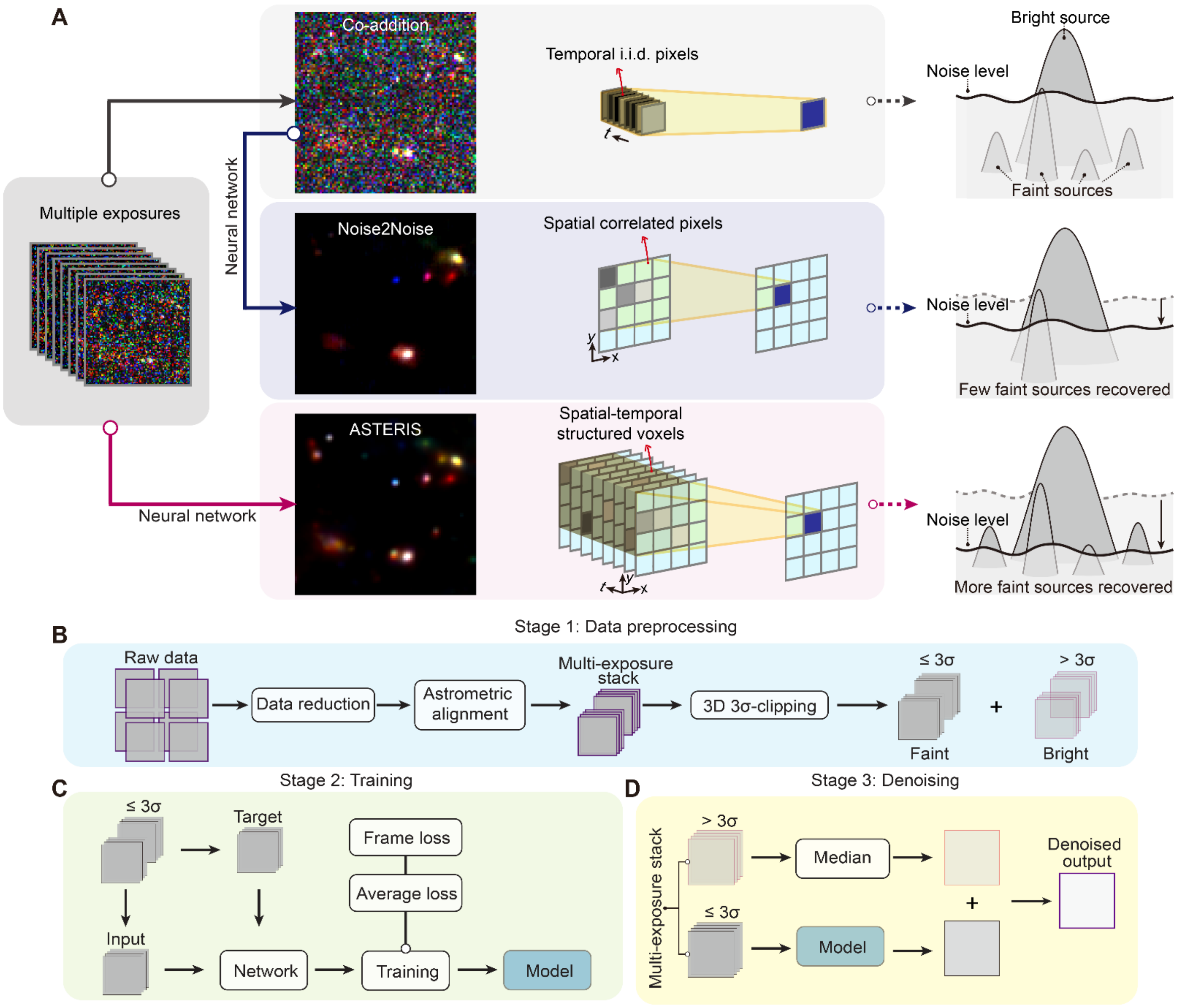

Fig. 1. Schematic overview of the ASTERIS algorithm. (**A**) Comparison between standard co-addition (outlier-rejected averaging), N2N denoising, and ASTERIS denoising. The columns from left to right illustrate the input data, denoising methods, underlying principles, and conceptual denoising effect. Solid lines denote data flow and dashed lines are the corresponding effect. In the third column, multi-colored grids illustrate the input noisy pixels in spatial (x, y) and temporal (t) dimensions, while the blue grid represents the resulting denoised pixel. Co-addition (top row with gray shading and arrows) increases the S/N by averaging multiple exposures under the assumption of independent pixel-level noise; however, faint signals remain below the residual noise fluctuations (standard deviation, std). The N2N deep-learning-based single-frame denoising method (middle, blue shading and arrows) reduces the noise std by modelling local spatial correlations, improving the S/N of bright sources (compared to co-addition) but recovering few additional faint sources. ASTERIS (bottom, pink shading and arrows) jointly processes multiple exposures, producing a single denoised frame by learning spatiotemporal correlations. This both reduces the noise std and recovers more previously undetectable faint sources. (**B**) Pre-processing in ASTERIS. Multiple exposures of the same pointing are combined after data reduction and astrometric alignment, then separated into a bright part and a faint part, using a 3σ clipping threshold. (**C**) Training of ASTERIS. The faint part of the image ($\leq 3\sigma$) is randomly sampled into input and target sets for self-supervised learning by a neural network. The model is trained to minimize both an average loss (MSE) and a frame loss (MAE) between the neural network output and the target exposures. (**D**) Denoising in ASTERIS. The faint part ($\leq 3\sigma$) of the multi-exposure image stack is denoised by ASTERIS, then recombined by co-adding the median of the bright part ($> 3\sigma$), to produce the final denoised image with full dynamic range.

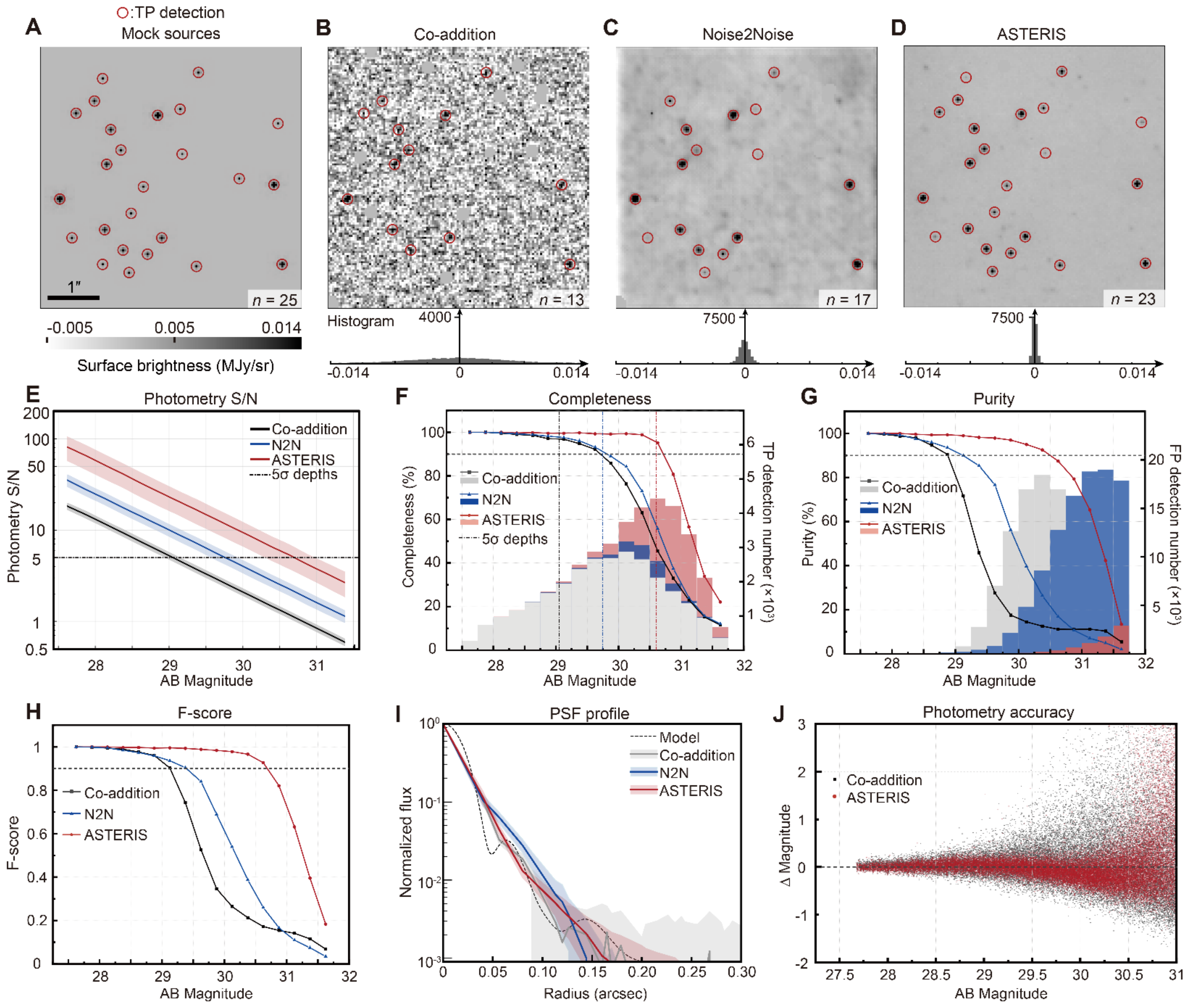

Fig. 2. Characterization of ASTERIS using mock sources. (**A**) Example mock sources with no background, serving as the ground-truth image. Red circles indicate true positive (TP) source detections using Source Extractor, counted by the labeled number *n*. The black scale bar is 1.0″ and the color bar is in megajansky per steradian (MJy sr^{-1}). (**B**) Image produced by co-addition of 8 exposures generated by injecting the mock sources in panel A into real background noise taken from JWST NIRCam F115W images. The same exposures were used as input for (**C**) N2N and (**D**) ASTERIS. The same Source Extractor parameters were used in each panel. Histograms below panels B-D show the corresponding pixel values, as a measure of the background noise variance. (**E**) Colored lines show the derived source-dependent photometric S/N after denoising using each method (see legend). Solid lines show the mean S/N, in 0.25 mag bins, from 50,000 injected sources; shaded regions indicate the ±1σ scatter. The horizontal dot-dash black line in panels E-F indicates the 5σ detection threshold. (**F**) Detection completeness (lines with data points) and number of true positives (histograms) for each method. The vertical black lines indicate the 90% completeness level using each method. (**G**) Same as panel F but for detection purity (lines) and number of false positives (histograms). The dashed line is at 90% purity. (**H**) The F-score metric (equation S7) for each method. The dashed line indicates F-score = 0.9. (**I**) The PSF profiles (colored lines) from each method, using 0.04″ pixel sampling. The model PSF (light gray) was generated using the STPSF software (*64*), sampled at 0.01″. (**J**) Comparison of photometric accuracy for the 50,000 mock sources, as measured using co-addition (black points) and ASTERIS (red points). The dashed black line indicates no difference between the mock injection and the derived measurement. The data in panels E, F, and J were all measured using 0.14″ radius circular apertures around the identified sources (*33*). Figure S6 shows another example in a larger and more crowded field.

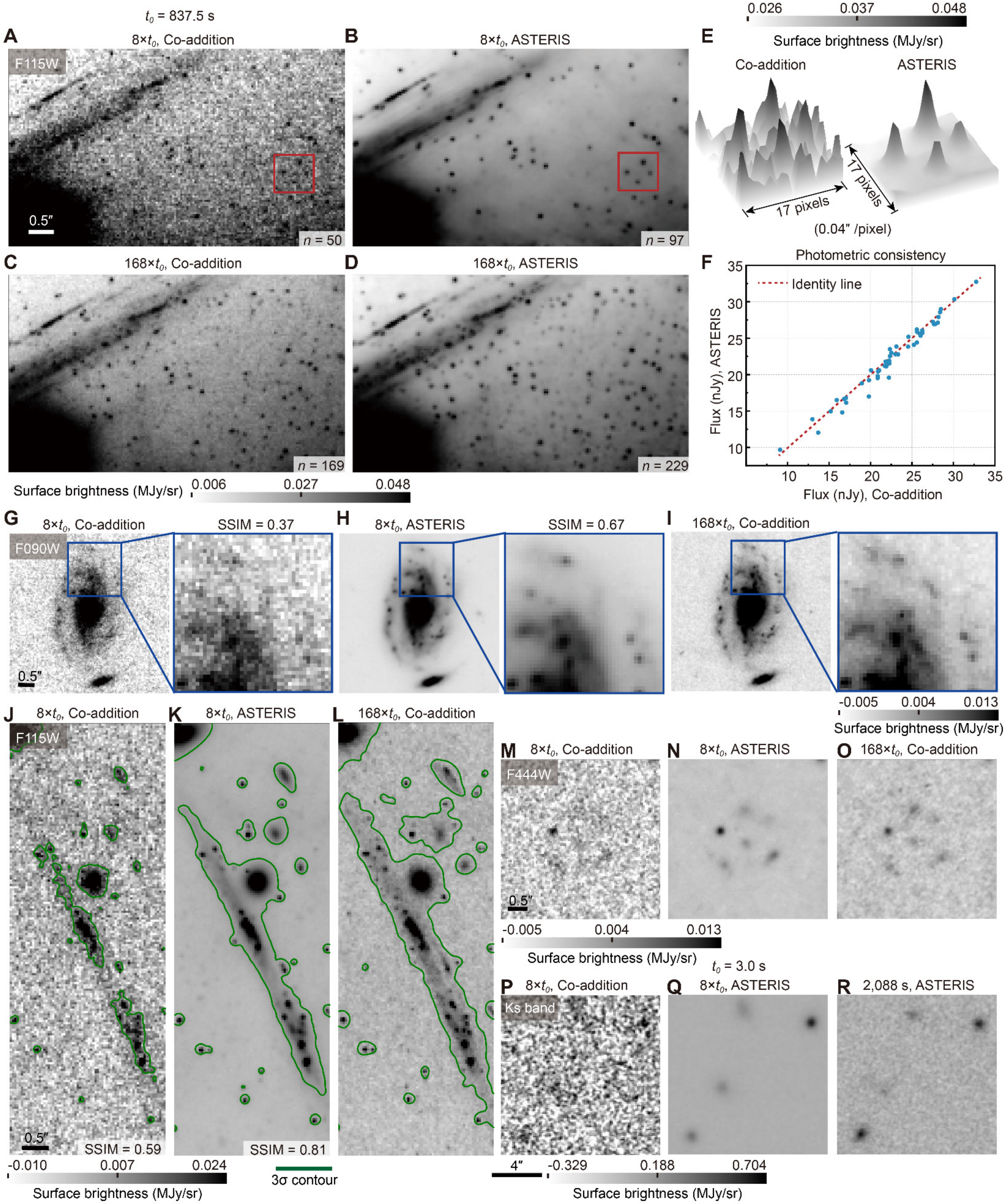
t_0 = 837.5 s
A
8×t_0, Co-addition
F115W
0.5″
n = 50
B
8×t_0, ASTERIS
n = 97
E
0.026
0.037
0.048
Surface brightness (MJy/sr)
Co-addition
ASTERIS
17 pixels
17 pixels
(0.04″ /pixel)
C
168×t_0, Co-addition
n = 169
D
168×t_0, ASTERIS
n = 229
Surface brightness (MJy/sr)
0.006
0.027
0.048
F
Photometric consistency
Identity line
Flux (nJy), ASTERIS
Flux (nJy), Co-addition
10
15
20
25
30
35
G
8×t_0, Co-addition
SSIM = 0.37
F090W
0.5″
H
8×t_0, ASTERIS
SSIM = 0.67
I
168×t_0, Co-addition
-0.005
0.004
0.013
Surface brightness (MJy/sr)
J
8×t_0, Co-addition
F115W
0.5″
SSIM = 0.59
K
8×t_0, ASTERIS
SSIM = 0.81
L
168×t_0, Co-addition
-0.010
0.007
0.024
Surface brightness (MJy/sr)
3σ contour
M
8×t_0, Co-addition
F444W
0.5″
N
8×t_0, ASTERIS
O
168×t_0, Co-addition
-0.005
0.004
0.013
Surface brightness (MJy/sr)
t_0 = 3.0 s
P
8×t_0, Co-addition
Ks band
Q
8×t_0, ASTERIS
R
2,088 s, ASTERIS
4″
-0.329
0.188
0.704
Surface brightness (MJy/sr)

Fig. 3. Observational validation of ASTERIS on real data. t_0 is the individual exposure time and $M\times$ indicates that M exposures were used. (**A** to **D**) A crowded field observation from JWST NIRCam in F115W, with t_0= 837.5 s. n is the number of sources identified by Source Extractor with fixed parameters. The images resulting from (**A**) co-addition of 8 × t_0 exposures, (**B**) ASTERIS applied to 8 × t_0 exposures, and (**C**) co-addition of 168 × t_0 exposures, serving as the ground truth for panels A and B. (**D**) ASTERIS applied to 168 × t_0 exposures, which shows fainter sources than the ground truth image in panel C. (**E**) 2D surface profiles of the region within the red-boxes in panels A and B. (**F**) Comparison of the measured fluxes for true-positive sources in panels A and B. The dotted red line indicates identical values in the two methods. (**G** to **I**) Similar to panels A-C, but for an example spiral galaxy observed using JWST NIRCam in F090W, with a zoom-in view of the spiral arms. The labeled SSIM values of the zoomed-in regions in panels G and H were computed relative to the image in panel I. (**J** to **L**) Similar to panels A-C, but for an example gravitational lensing arc, observed using JWST NIRCam in F115W. Green contours are at 3σ significance. The labeled SSIM values in panels J and K were computed inside the contours, relative to the image in panel L. (**M** to **O**) Similar to panels A-C, but for an example group of faint and diffuse galaxies observed using JWST NIRCam in F444W. (**P** to **R**) Similar to panels A-C, but for another group of faint sources observed using Subaru MOIRCS in *Ks*-band. For these data, t_0 = 3 s. (**R**) A co-addition with total exposure time of 2,088 s, serving as the ground truth for panels P and Q. The scale bars in panels A, G, J and M are 0.5″, and in panel P is 4″. Figure S13 shows a comparison of spatial profiles taken from the same three example JWST regions.

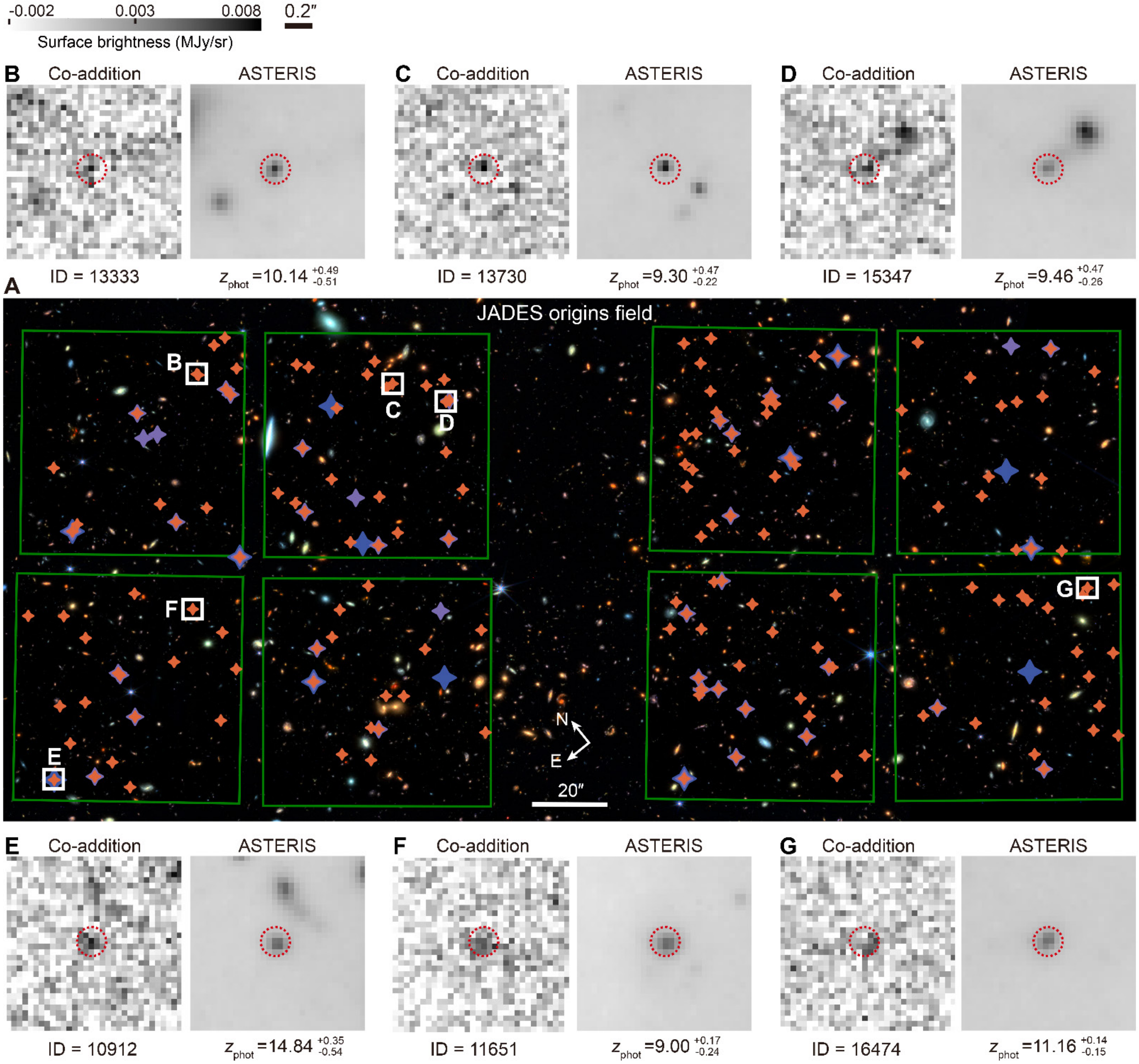

Fig. 4. Application of ASTERIS to faint high-redshift galaxy candidates in the JOF. (**A**) The background is a false-color RGB composite image of the JOF NIRCam imaging processed using ASTERIS; blue is F115W + F150W, green is F200W + F277W, and red is F356W + F444W. Green boxes outline the boundaries of the F200W image footprint. The scale bar is 20″. Diamond symbols indicate high-redshift galaxy candidates identified within the F200W footprint by previous studies [blue (*52*) and purple (*53*)] and in this study using ASTERIS (orange). The compass arrows indicate north and east. (**B**-**G**) Zoomed thumbnails of the candidates in the labeled white boxes in panel A. Each panel shows the two F200W images produced by standard co-addition and ASTERIS. Red dashed circles around the candidate sources are 0.2″ in diameter. z_{phot} is the best-fitting photometric redshift and the labeled ID numbers correspond to entries in table S3.

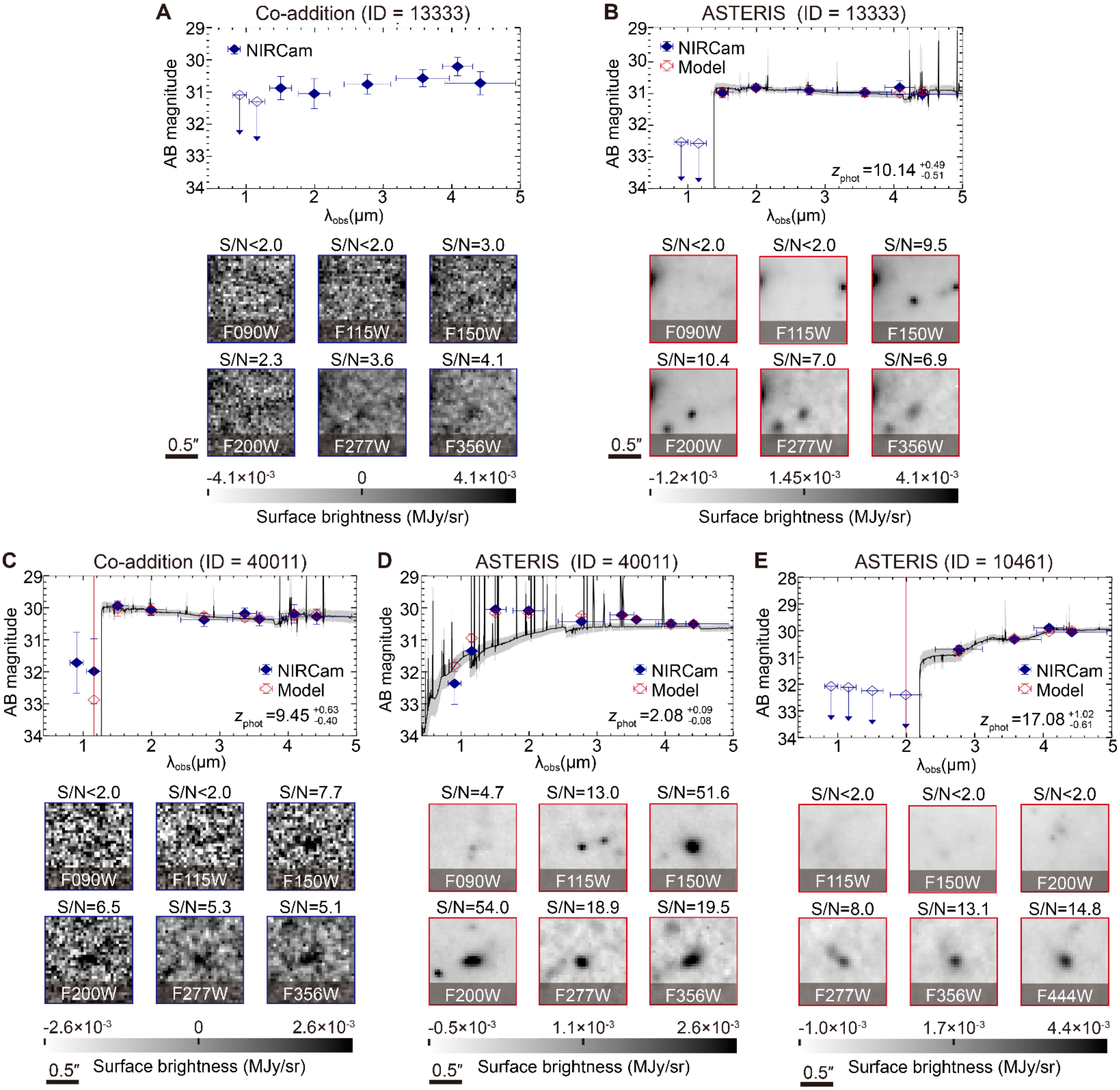

Fig. 5. Example high-redshift galaxy candidates identified using ASTERIS. Three example sources are shown, labeled with their ID number in table S3. Each panel plots the thumbnail images in each filter (below) and the corresponding spectral energy distribution (SED, above) (*33*). The scale bar in the thumbnail images is 0.5 arcseconds. The SED horizontal axes are the observed-frame wavelength λ_{obs}. Blue solid diamonds (with 1σ error bars) are the observed photometry. For filters with S/N < 1.0, 2σ upper limits are plotted as open blue diamonds with downward arrows. Black lines are model spectra fitted to the observations, gray shading is the 1σ model uncertainty, and red open diamonds are synthetic photometry computed from the model spectra. (A-B) Comparison of results from standard co-addition and ASTERIS for a faint F115W dropout candidate which is close to the detection limit in the co-addition image, which did not determine its redshift. ASTERIS improves the depth of the F090W and F115W photometry by > 1.0 mag, constraining its redshift. (C to D) Same as panels A-B but for a source with previously ambiguous redshift. The F090W photometry had S/N < 2.0 in the co-addition and S/N = 4.7 using ASTERIS, which changes the best-fitting redshift from z_{phot} = 9.45 to z_{phot} = 2.08. (E) Same as panel B but for a F200W-dropout high-redshift candidate which was identified in the ASTERIS image but not in the co-addition image. Figure S16 shows five additional examples.

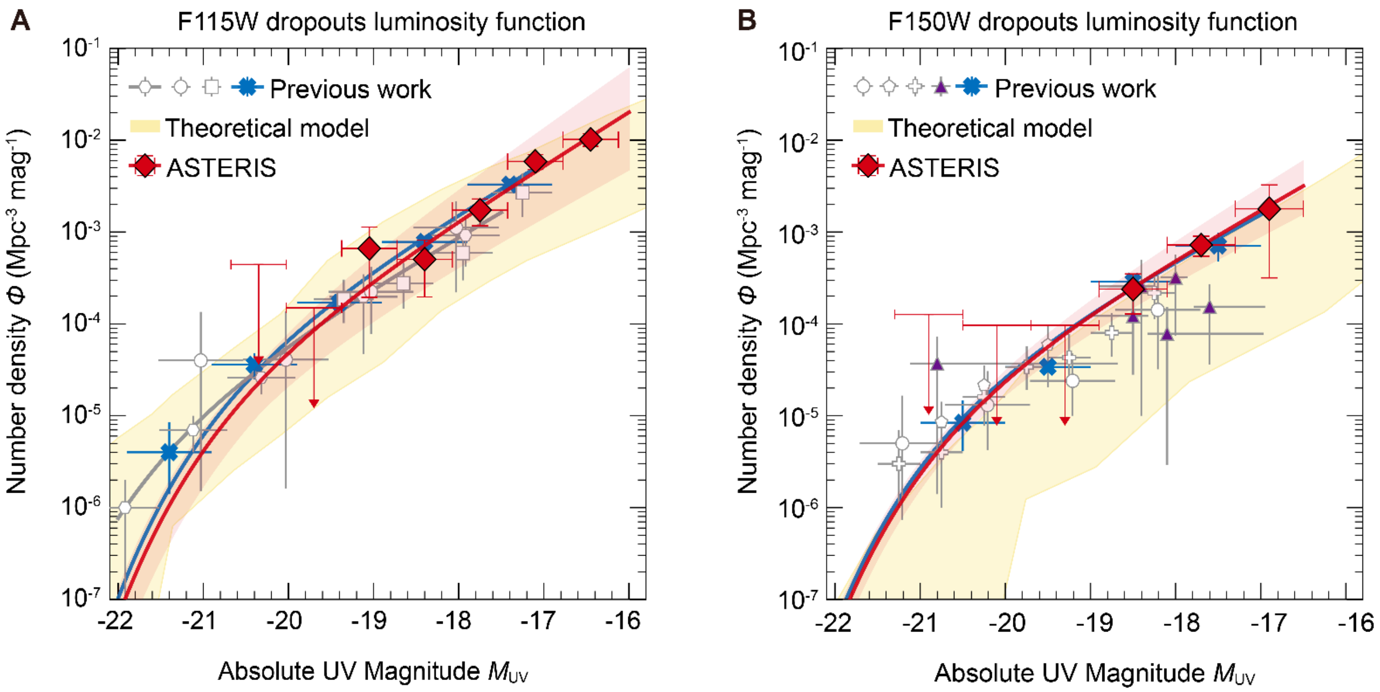

Fig. 6. Rest-frame UV luminosity functions of the high-redshift galaxy candidates in JOF. These luminosity functions are the galaxy number density Φ [galaxies per cubic megaparsec (Mpc) per magnitude] as a function of UV absolute magnitude M_{UV}. Red diamonds are the binned number densities from the ASTERIS photometry of the JOF. Red curves are models fitted to the data (*33*), with pink shading indicating their 1σ uncertainties. Blue squares show equivalent results from a previous analysis of the JOF using standard co-addition (*53*). Purple triangles are from another previous study of only F150W dropouts in the JOF (*52*). Gray symbols show results from previous studies of other fields [hexagons (*74*), circles (*75*), squares (*76*), pentagons (*77*), and crosses (*78*)]. The yellow shaded regions are theoretical predictions for F115W dropouts (*58*, *79*, *80*) and F150W dropouts (*57*, *81*, *82*). (A) F115W dropouts, corresponding to $z \sim 9$ to 12. The ASTERIS analysis of the JOF identifies 125 galaxy candidates in this range, with a median redshift of 9.51. (B) F150W dropouts, corresponding to $z \sim 12$ to 16. The ASTERIS analysis identifies 33 galaxy candidates in this range, with a median redshift of 12.97.

Deeper detection limits in astronomical imaging using self-supervised spatiotemporal denoising

Yuduo Guo, Hao Zhang, Mingyu Li, Fujiang Yu, Yunjing Wu, Yuhan Hao, Song Huang, Yongming Liang, Xiaojing Lin, Xinyang Li, Jiamin Wu, Zheng Cai, and Qionghai Dai

Science **Ahead of Print** DOI: 10.1126/science.ady9404

Science (ISSN 1095-9203) is published by the American Association for the Advancement of Science. 1200 New York Avenue NW, Washington, DC 20005. The title *Science* is a registered trademark of AAAS.